https://doi.org/10.5194/egusphere-2025-6284
Preprint. Discussion started: 7 April 2026

Shifting Drivers of China's Methane Emissions amid Economic Growth and Mitigation between 2019–2024

Yifan Li[1,2,3], Drew C. Pendergrass[2]†, Daniel J. Jacob[2], Yunxiao Tang[2], Jiaxin Qiu[1], Bo Zheng[1,3,*]

[1]Shenzhen Key Laboratory of Ecological Remediation and Carbon Sequestration, Institute of Environment and Ecology, Tsinghua Shenzhen International Graduate School, Tsinghua University, Shenzhen, 518055, China
[2]John A. Paulson School of Engineering and Applied Sciences, Harvard University, Cambridge, MA, 02138, USA
[3]State Environmental Protection Key Laboratory of Sources and Control of Air Pollution Complex, Beijing, 100084, China.
†Now at Nicholas School of the Environment, Duke University, Durham, NC, 27708, USA.

Correspondence to: Bo Zheng (bozheng@sz.tsinghua.edu.cn)

Abstract. Amid the accelerated growth in global atmospheric methane (CH_4) concentrations after 2019, identifying key emitting regions, quantifying their contributions, and elucidating the underlying drivers have become pressing needs. However, limited monitoring capacity and complex inversion systems have constrained the timely and accurate assessments of regional CH_4 emissions. Here, we construct a regional atmospheric inversion framework using the Local Ensemble Transform Kalman Filter (LETKF), constrained by satellite CH_4 observations. Applied to East Asia at 0.5° × 0.625° resolution, this system produces weekly CH_4 flux estimates for China during 2019–2024. We show that China's CH_4 emissions increased from 61.1 (56.2–66.7) Tg in 2019 to 66.8 (61.5–73.0) Tg in 2024. The livestock sector contributed nearly half of the growth, while rising waste and oil-gas emissions and northward expansion of rice cultivation shifted China's emissions growth to previously low-emitting Northwest and Northeast regions. Our framework demonstrates the feasibility of near-real-time, regional-scale emissions monitoring, offering a transferable tool for other high-emitting countries.

https://doi.org/10.5194/egusphere-2025-6284
Preprint. Discussion started: 7 April 2026

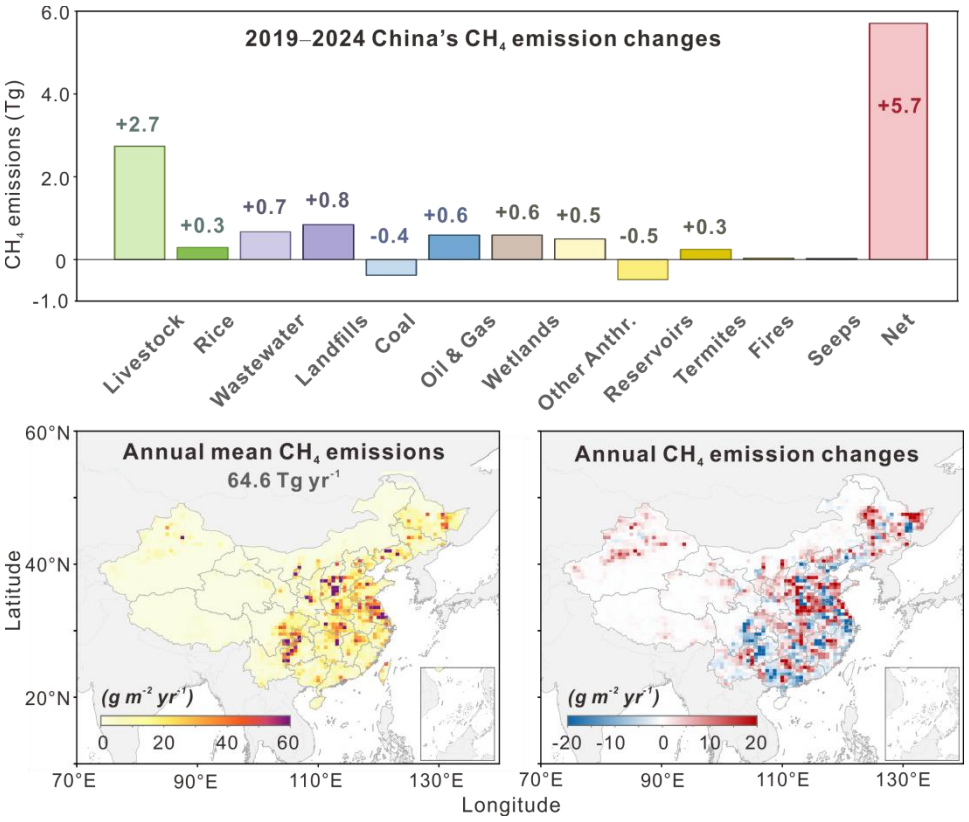

1 Introduction

Methane (CH_4) is a powerful greenhouse gas whose atmospheric concentrations have risen steadily in recent decades, with a marked acceleration after 2019 (Lan et al., 2025). Given its atmospheric lifetime of ~9 years and a 20-year global warming potential over 80 times that of carbon dioxide (CO_2), CH_4 mitigation has emerged as a priority for near-term climate action under the Paris Agreement (Intergovernmental Panel on Climate Change, 2023). In response, the Global Methane Pledge was launched in 2021, aiming to reduce global CH_4 emissions by at least 30% from 2020 levels by 2030 through enhanced national actions and international cooperation (Global Methane Pledge, 2023). Anthropogenic CH_4 emissions have more than doubled the atmospheric CH_4 burden since the industrial era and now account for nearly 60% of global total emissions, primarily from the fossil fuel, agriculture, and waste treatment sectors (Staniaszek et al., 2022; Saunois et al., 2025). Rapid and sustained control of major anthropogenic sources is widely considered an effective strategy for mitigating CH_4 emissions.

China, as the largest anthropogenic CH_4 emitter globally, accounts for approximately one-fifth of the global human emissions at present. According to its national emission inventory submitted to the United Nations Framework Convention on Climate Change (UNFCCC), fossil fuel emissions have dominated since the 2000s, followed by agriculture and waste sectors. CH_4 emission control has become a policy concern in China since 2007, when the National Plan on Climate Change

https://doi.org/10.5194/egusphere-2025-6284
Preprint. Discussion started: 7 April 2026

first emphasized its importance in key sectors. Over time, mitigation efforts have been reinforced through sector-specific policy measures and have become a key component of China's 'Dual Carbon' goal to achieve carbon neutrality by 2060. Since 2023, the development of a monitoring, reporting, and verification (MRV) system has been emphasized in China's first national CH_4 emissions control action plan, alongside more comprehensive and targeted guidance for CH_4 mitigation efforts (Ministry of Ecology and Environment of China, 2023). Emerging findings reveal a deceleration in China's CH_4 emissions growth after 2016 (Zhao et al., 2024); however, the absence of up-to-date estimates hampers the timely assessment of the national emissions landscape and the mitigation effectiveness. Therefore, a near-real-time tracking of CH_4 emissions, together with analyses of temporal trends and underlying drivers, is essential for tracking mitigation progress and supporting more adaptive and effective future management strategies.

Multiple estimation approaches have been employed to quantify regional CH_4 budgets. Bottom-up (BU) emission inventories provide sectoral details but suffer from evident uncertainties—owing to difficulties in obtaining complete activity data, developing localized emission factors, and accounting for comprehensive influence factors—and often lag several years behind (Crippa, 2024; Guo et al., 2025; Cui et al., 2025; Hoesly, 2025; Peng et al., 2016). Top-down (TD) approaches, particularly incorporating dense satellite observations, could improve emission estimates through Bayesian optimization (Saunois et al., 2025). Nevertheless, regional-scale TD inversions remain highly uncertain. For China, the emission estimates over the past decade vary widely from 35 to 70 Tg yr^{-1} across studies (Kou et al., 2025; Chen et al., 2022; Worden et al., 2022; Pendergrass et al., 2025; Janardanan et al., 2024; Zhao et al., 2024; Saunois et al., 2020; Guo et al., 2025; Saunois et al., 2025; East et al., 2025), and the current emission trends remain poorly constrained. Moreover, many regional satellite-based inversions have only targeted individual years (Chen et al., 2022; Kou et al., 2025), whereas multi-year trends are typically inferred from coarse-resolution global inversions that mask some regional emission signals (Qu et al., 2021; Zhao et al., 2024; Janardanan et al., 2024; Saunois et al., 2025). These limitations highlight the urgent need for consistent, low-bias, long-term observational datasets with comprehensive spatial coverage, as well as more efficient inversion tools capable of monitoring emissions at high spatiotemporal resolutions, to strengthen observational constraints and inversion frameworks.

Recent advances in satellite instrumentation and atmospheric inversion techniques offer opportunities to timely and efficiently monitor CH_4 emissions for China. The recently developed blended TROPOMI+GOSAT CH_4 retrieval product, based on machine learning to combine the high-resolution TROPOspheric Monitoring Instrument (TROPOMI) data (Lorente et al., 2021) with the high-precision but sparse Greenhouse Gases Observing Satellite (GOSAT) data, provides strong spatial and temporal constraints for regional inversions (Balasus et al., 2023). In parallel, the Local Ensemble Transform Kalman Filter (LETKF), a widely adopted extension of the ensemble Kalman filter (EnKF) (Hunt et al., 2007), enables efficient, iterative, and spatially localized optimization of emissions constrained by dense observations. The CHEmistry and Emissions REanalysis Interface with Observations (CHEEREIO) tool integrates the LETKF algorithm with the GEOS-Chem chemical transport model (CTM) and has been applied to global-scale inversions (Pendergrass et al., 2025; Voshtani et al., 2025).

https://doi.org/10.5194/egusphere-2025-6284
Preprint. Discussion started: 7 April 2026

Using this tool, Pendergrass et al. (2025) (Pendergrass et al., 2025) optimized global CH_4 emissions from 2019 to 2023 based on the blended TROPOMI+GOSAT CH_4 product.

Here, we develop a regional-scale CHEEREIO version to perform an inversion estimate of China's CH_4 fluxes from 2019 to 2024. This system optimizes weekly emissions at a horizontal resolution of 0.5° × 0.625°, constrained by the blended TROPOMI+GOSAT CH_4 column retrievals (Table 1). The results capture spatial and sectoral contributions of emissions at a high spatiotemporal resolution, offering insights into emission characteristics and the drivers of recent trends. To ensure the robustness of the inversion framework and estimation, we conducted a series of sensitivity tests on key parameter settings and model configurations. This study expands the methodological framework for regional inversions, enables timely and accurate tracking of CH_4 emissions, provides an independent and efficient evaluation of emission dynamics, and informs the formulation of targeted mitigation policies.

Table 1. Inversion system configuration.

Model setup	Configuration	Main references
Inversion setup		
Domain	10–60° N, 70–150° E	-
Spatial resolution	0.5° latitude × 0.625° longitude × 47 layers	-
Spin up period	2018/4/1–2018/10/01	-
Inversion period	2018/10/01–2024/12/31	-
Assimilation windows	7 days	-
Inversion algorithm	LETKF	(Hunt et al., 2007)
GEOS-Chem model		
Model version	14.3.1	-
Meteorological fields	MERRA-2	-
Prior information (*x*)		
CH_4 emissions	Fossil fuel: GFEI v2	(Scarpelli et al., 2022)
	Livestock: EDGARv7	(Crippa, 2021)
	Rice: EDGARv8 Waste: EDGARv8	(Crippa et al., 2023)
	Wetlands: LPJ-wsl with MERRA-2 met	(Zhang et al., 2016), (East et al., 2024)
	Hydroelectric reservoirs	(Delwiche et al., 2022)
	Termites	(Fung et al., 1991)
	Fire: GFED4	(Van Der Werf et al., 2017) (Randerson et al., 2017)
	Seeps	(Etiope et al., 2019), (Hmiel et al., 2020)
CH_4 sinks	Soil uptake: MeMo	(Murguia-Flores et al., 2018)
	OH fields	(Wecht et al., 2014)
	Cl fields	(Wang et al., 2019), (Mooring, 2024)
Observation vector (*y*)		
XCH_4 product	Blended TROPOMI+GOSAT CH_4	(Balasus et al., 2023)
Localization radius	Radius: 1500 km	-
Super observation	Transport error: 6.1 ppb Error correlation: 0.28 Error for a single retrieval: 17 ppb	(Pendergrass et al., 2023), (Pendergrass et al., 2025)

https://doi.org/10.5194/egusphere-2025-6284
Preprint. Discussion started: 7 April 2026

2 Methods

Our study conducts a regional CH_4 emission inversion over China (10–60° N, 70–150° E) from 2018 to 2024 based on the bias-corrected blended TROPOMI+GOSAT CH_4 retrieval product (Balasus et al., 2023) using the nested GEOS-Chem CTM with a resolution of 0.5° × 0.625°. We apply the LETKF algorithm to assimilate observations on a weekly scale via the CHEEREIO tool (Pendergrass et al., 2023). To evaluate our inversion estimates, we conduct a set of sensitivity tests examining key configurations and settings for the state vectors, GEOS-Chem model, error characterization, and assimilation process.

2.1 Satellite observations

TROPOMI, onboard the Sentinel-5 Precursor (S5P) satellite launched in October 2017, measures column-averaged dry-air methane mole fractions (XCH_4). These retrievals are derived from solar backscatter measurements in the 2.3 μm absorption band using a full-physics algorithm. XCH_4 retrievals are available globally on a daily basis at ~13:30 local solar time, with a nadir spatial resolution of 5.5 × 7 km^2 (7 × 7 km^2 prior to August 2019). Due to their dense and continuous CH_4 observations with high spatiotemporal resolution, TROPOMI data have been widely used in atmospheric CH_4 inversions. However, these retrievals may be affected by aerosols, shortwave infrared surface albedo, cirrus-cloud scattering, and across-track variability, which can introduce artifacts (Lorente et al., 2021). To mitigate these biases, we employed the blended TROPOMI+GOSAT methane product, which corrects TROPOMI biases using a machine-learning model trained on more precise but sparser GOSAT satellite data that uses a CO_2 proxy retrieval (Balasus et al., 2023). The TROPOMI+GOSAT retrievals exclusively use observations with the high-quality flag (qa = 1).

In our study, we exclude observation data over coastlines and oceans. After filtering, the blended TROPOMI+GOSAT product provides complete spatial coverage across China (Fig. 1). However, there are gaps in temporal coverage during specific periods due to the failure of the VIIRS instrument, which is used for cloud clearing, occurring between 26 July and 23 August 2022, 26 July and 30 August 2023, and 6 to 30 June 2024. To maintain temporal continuity, posterior emissions during these gaps are estimated using a gap-filling approach based on assimilation results from adjacent periods. Scaling factors produced by the LETKF algorithm are applied to the prior emissions to obtain optimized posterior estimates. For the missing periods, we calculate the mean scaling factors from m assimilation periods within one month before and n assimilation periods within one month after each interval, and use these averaged values to approximate the posterior emissions, as follows:

$$Posterior_{d,i} = \left(\frac{1}{m+n}\sum_{j=1}^{m+n} SF_{j,i}\right) \cdot Prior_{d,i}, \quad (1)$$

where $Posterior_{d,i}$ and $Prior_{d,i}$ are the posterior and prior CH_4 emissions, respectively, for grid cells i on assimilation period d within the missing period. $SF_{j,i}$ represents the scaling factor at grid cell i from valid assimilation on period j. m and n

https://doi.org/10.5194/egusphere-2025-6284
Preprint. Discussion started: 7 April 2026

represent the number of valid assimilation periods within the one-month windows before and after the missing period, respectively.

To reduce observation redundancy and ensure spatial consistency between satellite retrievals and the GEOS-Chem model grid cell, we aggregate overlapping satellite observations within each model grid cell into super-observations. These are calculated by averaging all valid observations within a given grid cell and an assimilation window (Chen et al., 2023; Pendergrass et al., 2025; Pendergrass et al., 2023; Eskes et al., 2003; Miyazaki et al., 2012; East et al., 2025). The corresponding observation error for each super-observation on the model grid is estimated using an error variance formulation (Eq. 2) that accounts for the uncertainty of individual native retrievals, the spatial correlation among retrievals within each grid cell, and the irreducible transport error.

$$\sigma_{super} = \sqrt{\left[\left(\frac{1}{p}\sum_{i=1}^{p}\sigma_i\right)\cdot\left(\frac{1-c}{p}+c\right)\right]^2 + \sigma_{transport}^2}, \quad (2)$$

where σ_{super} is the error standard deviation of a super-observation. σ_i is the error standard deviation of the i-th native retrieval contributing to that super-observation, and p is the number of individual observations aggregated into the super-observation. c is the assumed error correlation among retrievals within the same super-observation. σtransport represents the transport error of the forward model. The parameter settings follow the empirical residual error fitting approach applied in Chen et al. (2023) and Pendergrass et al. (2025) (Chen et al., 2023; Pendergrass et al., 2025).

2.2 GEOS-Chem forward model

GEOS-Chem is a three-dimensional CTM widely used for simulating atmospheric composition. Our study run the nested-grid simulations of the GEOS-Chem CTM (v14.3.1, https://zenodo.org/records/10908999) at 0.5° × 0.625° resolution over China (70–150° E, 10–60° N) as a forward model for methane assimilation. The model is driven by the Modern-Era Retrospective analysis for Research and Applications, Version 2 (MERRA-2) meteorological reanalysis fields of the NASA Global Modeling and Assimilation Office (GMAO). Boundary conditions in the simulation were modified using blended TROPOMI+GOSAT methane retrievals (Balasus et al., 2023), applied at 3-hour intervals. A spatiotemporal smoothing approach (Estrada et al., 2025) was employed to minimize systematic discrepancies between CH4 concentrations in the boundary conditions and observations.

Prior emissions in our CH_4 simulation are listed in Table 2. Non-fossil anthropogenic CH_4 emissions primarily originate from the Emissions Database for Global Atmospheric Research emission inventory version 8.0 (EDGARv8, https://edgar.jrc.ec.europa.eu/dataset_ghg80) (Crippa et al., 2023). We use EDGARv7 (Crippa, 2021) for livestock emissions instead of EDGARv8, due to anomalous spatial distributions in EDGARv8 where emissions are concentrated in a small number of grid cells in China with extremely strong emissions. Prior fossil fuel CH_4 emissions are based on the Global Fuel Exploitation Inventory version 2 (GFEI v2) (Scarpelli et al., 2022). For natural emissions, we use prior wetland emissions

https://doi.org/10.5194/egusphere-2025-6284
Preprint. Discussion started: 7 April 2026

from the Lund–Potsdam–Jena Wald Schnee und Landschaft (LPJ-wsl) dynamic global vegetation model driven by MERRA-2 assimilated meteorological fields (Zhang et al., 2016; East et al., 2024). Emissions from hydroelectric reservoirs, termite, and biomass burning emissions are sourced from Delwiche et al. (2022) (Delwiche et al., 2022), Fung et al. (1991) (Fung et al., 1991), and the Global Fire Emissions Database version 4 (GFED4) (Van Der Werf et al., 2017; Randerson et al., 2017), respectively. Geological seep emissions are sourced from Etiope et al. (2019) (Etiope et al., 2019) and scaled globally to match the annual total by Hmiel et al. (2020) (Hmiel et al., 2020). CH_4 sinks in the simulation include soil uptake and oxidation by OH and Cl radicals. CH_4 soil absorption is derived from the Soil Methanotrophy Model (MeMo) (Murguia-Flores et al., 2018). CH_4 loss from tropospheric OH oxidation is calculated using global 3-D OH fields from GEOS-Chem CTM (Wecht et al., 2014). Tropospheric and stratospheric Cl fields are sourced from Wang et al. (2019) (Wang et al., 2019) and Mooring et al. (2024) (Mooring, 2024). Average annual total and sectoral prior CH_4 emissions are summarized in Table 2.

Table 2. Annual mean prior and posterior CH_4 emissions and their changes across sectors in China during 2019–2024.

	Annual mean prior emissions (Tg yr^{-1})	Annual mean posterior emissions (Tg yr^{-1})	2024 posterior - 2019 posterior (Tg)
Net	**68.4**	**64.6**	**5.7**
Anthropogenic	64.3	60.5	5.4
Livestock	8.4	8.9	2.7
Rice	13.8	13.1	0.3
Wastewater	9.8	8.9	0.7
Landfills	6.0	5.4	0.8
Coal	21.1	18.6	-0.4
Oil & Gas	1.2	1.6	0.6
Others	4.1	4.0	0.6
Natural	6.1	6.0	0.3
Wetlands	2.1	2.3	0.5
Reservoirs	3.2	2.7	-0.5
Termites	0.7	0.8	0.3
Fires	0.2	0.2	0.0
Seeps	0.1	0.1	0.0
Soil absorption	-2.0	-2.0	0.0

** Annual mean prior emissions cover different time periods by source: 2019–2021 for livestock; 2019–2022 for rice, wastewater, landfills, and other anthropogenic sources; 2019–2023 for fires; and are constant for coal, oil and gas, wetlands, reservoirs, termites, and seeps.*
† Annual mean posterior emissions refer to the period 2019–2024.

https://doi.org/10.5194/egusphere-2025-6284
Preprint. Discussion started: 7 April 2026

2.3 LETKF algorithm

We apply the LETKF algorithm for data assimilation to optimize regional CH_4 emissions through minimizing the Bayesian scalar cost function [17], as shown in Eq. (3):

$$J(x) = (x - x^b)^{\mathrm{T}}(P^b)^{-1}(x - x^b) + \gamma(y - H(x))^{\mathrm{T}}R^{-1}(y - H(x)), \quad (3)$$

where x is the state vector to be optimized, and x^b is the prior (background) state vector, which consists of gridded emission scaling factors at a spatial resolution of 0.5° × 0.625° over land areas within our study domain, comprising a total of 8 290 elements. P^b is the prior (background) error covariance matrix. y represents observations from the blended TROPOMI + GOSAT product. $H(\bullet)$ is the observation operator that transforms state vectors into observation fields. R is the observational error covariance matrix. γ is the regularization factor accounting for unresolved error correlations. Through minimizing the cost function ($\Delta J(x) = 0$), we obtain the optimized posterior state vector x^a.

LETKF optimizes the cost function through an ensemble approach. We randomly initialize m ensemble members, each driven by gridded emission scaling factors sampled from an approximate multivariate normal distribution centered around 1. These scaling factors are multiplied by prior emissions, generating m distinct ensemble members that are propagated forward using the GEOS-Chem model over a 7-day assimilation window in parallel. We use sensitivity simulations to diagnose the influence of the magnitude of these initial perturbations on inversion results (Sect. 2.5).

The LETKF algorithm is detailed described referred to Pendergrass et al. (2025) (Pendergrass et al., 2025). In the framework, the prior error covariance matrix P^b is emulated based on the ensemble spread, with the perturbation X_i^b of each ensemble member *i* calculated as:

$$\overline{x^b} = \frac{1}{\mathrm{m}}\sum_{i=1}^{\mathrm{m}} x_i^b, \quad (4)$$

$$X_i^b = x_i^b - \overline{x^b}, \quad (5)$$

These perturbations form the prior perturbation matrix X^b:

$$X^b = [X_1^b, X_2^b, \ldots, X_m^b] \in \mathbb{R}^{n\times m}, \quad (6)$$

where *m* is the ensemble number (set to 24 and assessed with sensitivity tests in Sect. 2.5), *i* indexes the ensemble member and corresponding column of the perturbation matrix, and *n* is the length of the prior state vector, which is 8,290 in our inversion.

We apply the observation operation $H(\bullet)$ to each prior ensemble member to construct corresponding background vectors of simulated TROPOMI observations:

$$y_i^b = H(x_i^b), \quad (7)$$

https://doi.org/10.5194/egusphere-2025-6284
Preprint. Discussion started: 7 April 2026

Here the y_i^b are constructed so that the model state aligns in time with a corresponding TROPOMI observation, within ±1 hour. The LETKF is a localized algorithm, with emissions from each grid cell optimized independently based on observations only within a certain radius (1500 km in this study, consistent with Pendergrass et al. (2025) (Pendergrass et al., 2025)). We use a distance-weighted scheme based on the Gaspari-Cohn function (Gaspari and Cohn, 1999) to reduce influences of more distant observations.

The observation perturbation matrix Y^b is constructed column-wise by:

$$\overline{y^b} = \frac{1}{\mathrm{m}} \sum_{i=1}^{\mathrm{m}} y_i^b \,, \tag{8}$$

$$Y_i^b = y_i^b - \overline{y^b} \,, \tag{9}$$

$$Y^b = [Y_1^b, Y_2^b, \ldots, Y_m^b] \in \mathbb{R}^{p \times m} \,, \tag{10}$$

where p denotes the number of simulated observation elements.

Using the prior state and observation perturbation matrices X^b and Y^b, we compute the posterior ensemble mean and perturbations (Pendergrass et al., 2025; Hunt et al., 2007). The analysis (posterior) error covariance matrix $\widetilde{P^a} \in \mathbb{R}^{m \times m}$ is computed in a subspace:

$$\widetilde{P^a} = [(\gamma (Y^b)^{\mathrm{T}} R^{-1} Y^b + \ (\mathrm{m} - 1) \bullet I]^{-1} \,, \tag{11}$$

where $\widetilde{P^a} \in \mathbb{R}^{m \times m}$, I is the identity matrix of size m × m, and the regularization parameter γ is set to 0.1 (Pendergrass et al., 2025). Sensitivity simulations (Sect. 2.5) were conducted to test the impact of different values of γ on assimilation results. The posterior ensemble mean and posterior perturbation matrix are given by

$$\overline{x^a} = \overline{x^b} + \ \gamma X^b \widetilde{P^a} (Y^b)^T R^{-1} (y - \ \overline{y^b}) \,, \tag{12}$$

$$X^a = X^b [(\mathrm{m} - 1) \widetilde{P^a}]^{1/2} \,, \tag{13}$$

Each posterior ensemble member is then constructed by combining the posterior mean $\overline{x^a}$ with the corresponding column of the posterior perturbation matrix X^a.

$$x_i^a = \overline{x^a} + X_i^a \,, \tag{13}$$

The resulting ensemble $\{x_i^a\}_{i=1}^m$ provides updated gridded scaling factors, which are employed to prior emissions to derive posterior CH_4 emissions in the target domain and are subsequently applied as the prior input for the GEOS-Chem model in the next assimilation cycle.

In our ensemble-based inversion, the spread among ensemble members may collapse over time (Pendergrass et al., 2023; Pendergrass et al., 2025). To maintain appropriate ensemble spread during assimilation, we implement the Relaxation to

https://doi.org/10.5194/egusphere-2025-6284
Preprint. Discussion started: 7 April 2026

Prior Spread (RTPS) inflation approach to the analysis perturbation matrix (Pendergrass et al., 2025; Bisht et al., 2023), and evaluated the setting through sensitivity tests (Sect. 2.5) (Whitaker and Hamill, 2012).

2.4 Regional inversion by the CHEEREIO tool

CHEEREIO is a lightweight framework that integrates the GEOS-Chem CTM with the LETKF algorithm (https://cheereio.readthedocs.io). It automatically and continuously optimizes emission estimates over time by minimizing discrepancies between model-simulated and observed atmospheric concentrations. The software design and implementation are detail demonstrated in Pendergrass et al. (2023) (Pendergrass et al., 2023).

The CHEEREIO tool has been applied to global-scale inversions for CH_4 and air pollutants (Pendergrass et al., 2023; Pendergrass et al., 2025; Voshtani et al., 2025). Our study extends its application to a user-defined regional domain for the first time, using China as a case study for CH_4 inversion. A nested-grid GEOS-Chem forward simulation only for methane is performed over the domain (70–150° E, 10–60° N) at a spatial resolution of 0.5° × 0.625°. A six-month spin-up (May–October 2018) is applied, followed by a global scaling of CH_4 concentrations in the initial state to ensure consistency between the ensemble mean and observed background levels. The assimilation is then conducted from November 2018 to December 2024. Observations from the blended TROPOMI+GOSAT satellite product that fall outside the defined regional domain are excluded prior to assimilation to avoid artificial concentration gradients near the model boundaries, where no simulated data are available.

In our regional inversion, prior errors are assumed to follow a normal distribution. We found that, compared to lognormal assumptions, the normal distribution yields more stable posterior scaling factors, particularly in areas with sparse observational constraints or low prior magnitudes. Our inversion system optimizes only emission sources. To prevent negative emissions, which are unlikely to occur for CH_4 in our domain, we impose a minimum scaling factor of 0.001, but this unavoidably introduces a slight bias in the results, as the probability density functions are truncated. We calculate posterior total emission estimates by applying the updated gridded scaling factors to the prior total emissions, and likewise, infer posterior sectoral emissions by applying gridded scaling factors to prior sectoral emissions. The scaling factors are updated after each assimilation window (one week in this study). We emulate the initial prior error distribution across our ensemble by applying randomized gridded scaling factors to the prior emissions for each ensemble member. These factors are initially sampled from a multivariate normal distribution, with spatial correlations defined by an exponential decay function based on the distance, which is 100 km in our inversion.

2.5 Sensitivity tests

We conduct a suite of 14 experiments to assess the robustness and uncertainty of our inversion framework, as well as the sensitivity of posterior estimates to key modeling parameters (Table 3). These tests are designed to isolate the influence of specific components in the inversion system, grouped into four categories: (1) state vector setting, (2) GEOS-Chem

https://doi.org/10.5194/egusphere-2025-6284
Preprint. Discussion started: 7 April 2026

configuration, (3) error characterization, and (4) assimilation configuration. Each test alters one component relative to the base inversion, allowing a controlled evaluation of its isolated effect on posterior estimates. We report overall uncertainty using the spread of ensemble results, defined as the range of mean deviations between each ensemble member and the base simulation, which is larger than the posterior error estimated with the LETKF algorithm.

Table 3. Settings of sensitivity tests for the CH_4 inversion system.

Category	No.	Name	Setting description
State vector setting	1	GFEIv3	Replacing the prior fossil fuel emissions from GFEIv2 with GFEIv3.
	2	GRPI	Replacing the prior rice emissions from EDGARv8 with GRPI.
GEOS-Chem configuration	3	Scaled_BC	Modifying the boundary conditions generated based on scalars from the Global inversion
Error characterization	4	Lognormal	Switching the prior error distribution for scaling factors from normal to lognormal.
	5	Spread_0.05	Reducing the initial standard deviation of scaling factors from 0.15 to 0.05.
	6	Spread_0.5	Increasing the initial standard deviation of scaling factors from 0.15 to 0.5.
	7	Gamma_0.01	Reducing the regularization factor from 0.1 to 0.01
	8	Gamma 0.2	Increasing the regularization factor from 0.1 to 0.2
	9	Gamma 1.0	Increasing the regularization factor from 0.1 to 1.0
	10	RTPS_0.5	Reducing the RTPS parameter from 0.7 to 0.5.
	11	RTPS_1.0	Increasing the RTPS parameter from 0.7 to 1.0.
Assimilation configuration	12	Ens_12	Reducing ensemble size from 24 to 12 members.
	13	Ens_36	Increasing ensemble size from 24 to 36 members.
	14	RIP	Extending the observation window from 7 days to 14 days for 7 day assimilation frequency.

2.5.1 State vector setting

Within the LETKF framework, prior emissions serve as state vectors during the assimilation. They provide sectoral information for model simulation and emission allocation. Our study tests different prior inputs for fossil fuel sources and the rice cultivation sector to analyse the sensitivity of posterior results to different prior inventories. Fossil fuels emitted the dominant CH_4 in China, accounting for nearly 40% of China's anthropogenic CH_4 emissions (Crippa, 2024). Here, we compare two versions of the Global Fuel Exploitation Inventory (GFEI) as prior inputs: GFEI v2 (Scarpelli et al., 2022) (the base case) and GFEI v3 (Scarpelli et al., 2025) (GFEIv3 in Table 3). Compared with GFEI v2, GFEI v3 reflects substantial updates in both emission magnitudes and spatial distributions. It incorporates updated national emissions reported to the UNFCCC and employs improved spatial allocation based on newly available geospatial datasets, including the Oil and Gas Infrastructure Mapping database (OGIM) v1 for oil and gas infrastructure and the Global Energy Monitor's Global Coal Mine Tracker (GCMT) for coal mine locations. In addition, a new bottom-up methodology is used to estimate mine-level coal CH_4 emissions (Scarpelli et al., 2022; Scarpelli et al., 2025). In particular, China exhibits pronounced spatial discrepancies between GFEI v2 and GFEI v3. For rice cultivation, we conducted a comparative analysis using the Global Rice Paddy Inventory (GRPI) (Chen and Jacob, 2025) as an alternative prior, as our base prior rice emission from

https://doi.org/10.5194/egusphere-2025-6284
Preprint. Discussion started: 7 April 2026

EDGARv8 is much higher than other previous studies (Fig. S12). The two inventories exhibit large differences in both spatial patterns and inter-annual variability.

2.5.2 GEOS-Chem configuration

Boundary conditions, which provide background concentrations at the domain edges, are particularly important for long-lived gases such as CH_4 in nested GEOS-Chem simulations, as they directly influence the accuracy of forward model simulations. Our simulation applied bias-corrected and smoothed boundary conditions based on TROPOMI observations (Estrada et al., 2025). To assess the sensitivity of inversion to boundary fields, we perform an additional experiment using other boundary fields generated based on globally optimized CH_4 scaling factors produced by a global CH_4 assimilation at 2.0° × 2.5° resolution for 2018–2023 (Scaled_BC) (Pendergrass et al., 2025). These boundary fields incorporate corrections to prior concentrations, but residual biases—particularly during the early stages of the assimilation period—are difficult to eliminate entirely. We compare the simulated concentrations and posterior emissions based on the different boundary conditions to quantify their influence on the assimilation results.

2.5.3 Error characterization

The specification of prior errors and initial ensemble spreads determines the relative weighting between model simulations and observations during data assimilation, thereby influencing the magnitude and spatial structure of posterior corrections. We perform a series of sensitivity experiments to evaluate how error characterization and propagation affect the results. To examine the influence of error distribution, we compared a lognormal prior error distribution assumption (Lognormal) against the baseline normal distribution, using a fixed regularization factor of 0.1. Implementation of lognormal LETKF assimilation is given in Pendergrass et al. (2025) (Pendergrass et al., 2025).

We also experimented with different spreads of initial scaling factors, used to initialize the ensemble members with varying methane emissions. We adjusted the default spread parameter value of 0.15 to 0.05 (Spread_0.05) and 0.5 (Spread_0.5), representing narrower and broader initial prior error spreads, respectively. We further assess the role of the regularization factor γ, a key parameter controlling the relative strength of observational constraints in the cost function (Eq. 1), by testing values of 0.01, 0.2, and 1.0. Higher values of γ imply stronger observational constraints, while lower values favor prior emissions. Additionally, we explored the treatment of error propagation by comparing RTPS values of 0.5 (RTPS_0.5) and 1.0 (RTPS_1.0) against the default setting of 0.7 (Pendergrass et al., 2025).

2.5.4 Assimilation configuration

The ensemble in the LETKF framework determines the representation of the background error covariance (Eqs. 4–6), which in turn affects the calculation of the Kalman gain and the posterior updates (Eqs. 12 and 13). Larger ensembles offer improved error structures and reduced sampling noise, but have higher computational demands. In addition to the baseline

https://doi.org/10.5194/egusphere-2025-6284
Preprint. Discussion started: 7 April 2026

setup with 24 ensemble members, we conducted experiments using 12 (Ens_12) and 36 (Ens_36) members to examine the effects of ensemble size on the quality and stability of the inversion results. The influence of the observational window length was further evaluated using the run-in-place (RIP) assimilation mode (Kalnay and Yang, 2010; Liu et al., 2019). Our study uses a longer observational window of 14 days to update emissions over a 7-day assimilation window. This method allows more temporal information to be assimilated during each assimilation period and is detailed described in Pendergrass et al. (2025) (Pendergrass et al., 2025).

3 Results and discussion

3.1 Evaluation of prior and posterior CH_4 simulations

We utilized blended TROPOMI and GOSAT satellite observations to optimize weekly CH_4 fluxes derived from prior estimates, which are available mostly at an annual resolution. A total of 22 047 486 quality-assured satellite retrievals over the land area of the GEOS-Chem domain were assimilated between 2019 and 2024 (Fig. 1a). The observations exhibited dense spatial coverage over the Northeast, Northwest, North, as well as parts of East China (the region split referred to Table S1 and Fig. S1). The satellite observations show elevated XCH_4 over China, with a multi-year mean of 1884.1 ppb (Figs. 1a and 1b), and hotspots primarily located in Southwest, South, East, and North China.

In our inversion system, we optimized surface emission fluxes such that the updated emissions applied in forward simulations improve the simulation performance of CH_4 concentrations. Over the study domain (70–150° E, 10–60° N), both satellite observations and GEOS-Chem simulations based on prior and optimized emissions exhibited increasing XCH_4 trends, while their discrepancies remained small owing to the application of smoothed boundary conditions that represent CH_4 levels outside the domain well (Fig. 1a). We conducted a detrended correlation analysis between observed and simulated XCH_4 based on prior and optimized emissions at grid level across China over the entire study period (Figs. 1c and 1d). A higher detrended correlation coefficient indicates stronger consistency between observations and model simulations. After assimilation, the correlations were consistently strengthened over the period 2019–2024 (Fig. 1c). The mean correlation increased slightly from 0.74 to 0.75, while the proportion of grid cells with correlations exceeding 0.7 rose from 69.8% to 73.9%. The majority of improved grid cells were located in South, East, and North China, which collectively contribute approximately 60% of national CH_4 emissions in total, indicating enhanced satellite observation constraints over key emission regions.

We further evaluated the simulated surface CH_4 concentrations against observations from the Observation Package (ObsPack) dataset (obspack_ch4_1_GLOBALVIEWplus_v7.0_2024-10-29) between 2019 and 2023 (Schuldt et al., 2024). Observations from five surface sites located in East Asia were used in the comparison, as summarized in Table S2. Across all sites, the Pearson correlation coefficient (r) between posterior and observed concentrations exceeded 0.6. A notable improvement was observed at the Anmyeon-do (AMY) station, where *r* increased from 0.55 in the prior to 0.61 in the

https://doi.org/10.5194/egusphere-2025-6284
Preprint. Discussion started: 7 April 2026

posterior, and at the Tae-ahn Peninsula (TAP) site, where the mean bias was decreased from 5.5 ppb to 2.3 ppb. However, the improvements were limited at the other sites, possibly due to transport errors associated with coarse model resolution, which constrain the inversion's ability to enhance agreement at sub-grid scales. In addition, many stations are located in coastal regions where our inversion exerts relatively weak constraints, and observational coverage is sparse during the study period. An exception was the Ryori (RYO) station, where dense observational coverage enabled CH_4 concentrations in our inversion to match ObsPack measurements, yielding a correlation of over 0.8 in both the prior and posterior simulations. The future efforts could expand the observation network and strengthen the joint assimilation of surface and satellite observations, providing more effective constraints on China's CH_4 emissions (Lu et al., 2021).

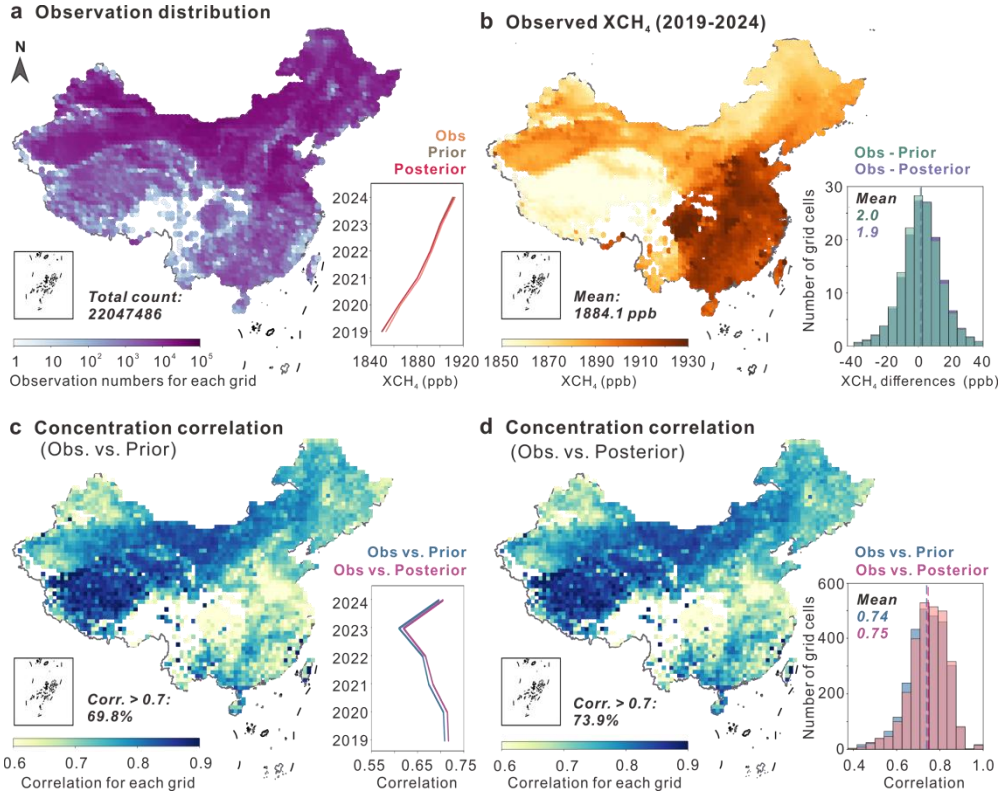

Figure 1: TROPOMI methane (CH_4) observations and spatial concentration correlation analysis with GEOS-Chem simulations. (a) Spatial coverage and number of TROPOMI observations across China during 2019–2024. The inset line plot shows annual XCH_4 from observations (Obs), and from prior and posterior simulations. (b) Mean gridded XCH_4 from TROPOMI observations across China from 2019 to 2024. The inset histogram shows the distribution of grid-level differences between observations and simulations. (c and d) Detrended spatial correlations between observations and prior (c) or posterior (d) simulations. The inset line plot in (c) shows annual mean correlation coefficients over China between observed and simulated XCH_4. The inset histogram in (d) shows the distribution of grid-level detrended correlation coefficients for observed and simulated XCH_4.

https://doi.org/10.5194/egusphere-2025-6284
Preprint. Discussion started: 7 April 2026

3.2 Inversion estimates of China's CH_4 fluxes during 2019–2024

We optimized China's weekly CH_4 fluxes from 2019 to 2024 (Fig. 2a) and found that prior emissions overestimated CH_4 emissions throughout the study period. The LETKF made larger emissions adjustments in spring, summer, and winter than in autumn. Both prior and posterior emissions exhibit pronounced seasonality, with a peak in summer and a minimum in winter (Fig. 2a). This seasonal cycle is primarily driven by rice cultivation, with a smaller contribution from wetlands (Fig. S2). Aggregated from the weekly fluxes, our annual average CH_4 fluxes for China across 2019–2024 are 64.6 (59.4–70.6) Tg yr^{-1} (the uncertainty ranges based on sensitivity tests). Annual CH_4 fluxes steadily increased from 61.1 (56.2–66.7) Tg in 2019 to 66.8 (61.5–73.0) Tg in 2024 (Fig. 2b). China's CH_4 emissions are broadly dispersed, with hotspots observed in East (15.2 Tg yr^{-1}), South (13.8 Tg yr^{-1}), Southwest (11.7 Tg yr^{-1}), and North China (10.4 Tg yr^{-1}), whereas the notable increase occurred in the Northwest (+2.7 Tg) and Northeast China (+1.9 Tg) (Figs. 2c and 2d).

Compared with the existing top-down estimates (Fig. 2e), our annual results are in close agreement with GONGGA-CH_4 (Zhao et al., 2024) and Janardanan et al. (2024) (Janardanan et al., 2020), but approximately 6.4% lower than Chen et al. (2022) (Chen et al., 2022) and 6.3% higher than Li et al. (2025) (Li and Zheng, 2025). Our estimates tend to be higher than the results from global inversions, including the ensemble inversions from Global Carbon Project (GCP) (Saunois et al., 2025), Worden et al. (2022) (Worden et al., 2022), and Qu et al. (2021) (Qu et al., 2021). These discrepancies likely stem from our higher spatiotemporal resolution, improved satellite data with corrected boundary conditions, and different priors. The blended TROPOMI+GOSAT product integrates the extensive spatiotemporal coverage of TROPOMI with the high precision of GOSAT, providing more comprehensive and reliable observational constraints for inverse modeling compared with using either dataset alone in previous studies (Balasus et al., 2023).

Anthropogenic CH_4 emissions account for 91.0% of China's total emissions during 2019–2024, with an average of 60.5 (53.7–65.1) Tg yr^{-1}. Compared with bottom-up estimates, our inversion-based anthropogenic emissions fall within the broad range, despite the prior being relatively high (Fig. 2f). Our posterior results are consistent with those from the People's Republic of China Fourth Biennial Update Report on Climate Change in 2020 (60.4 Tg in 2020) (Ministry of Ecology and Environment of China, 2024), and the Emissions Database for Global Atmospheric Research (EDGAR_2024) (Crippa, 2024). Our results are 12.5–16.6% lower than the estimates from the Food and Agriculture Organization (FAO) (Food and Agriculture Organization of the United Nations, 2025) and EDGARv8 (Crippa et al., 2023), and are 15.8%–23.4% higher than CEDSv2025_03_18 (Hoesly, 2025) and PKU-CH_4 v2 (Peng et al., 2016; Liu et al., 2021).

Our results revealed a post-2019 CH_4 emission growth in China. During 2013–2018, existing top-down studies reported an average increasing trend of 0.2 ± 0.4 Tg yr^{-2} (mean ± 1 standard error) in total CH_4 fluxes (Janardanan et al., 2020; Zhao et al., 2024; Saunois et al., 2025), whereas bottom-up inventories showed a decreasing trend of -0.3 ± 0.4 Tg yr^{-2} in anthropogenic emissions (Hoesly, 2025; Crippa, 2024; Crippa et al., 2023; Peng et al., 2016; Cui et al., 2025; Liu et al., 2021; Fao, 2024) (Table S3), based on non-parametric Mann-Kendall tests. In comparison, our posterior results for the subsequent

https://doi.org/10.5194/egusphere-2025-6284
Preprint. Discussion started: 7 April 2026

period 2019–2024 revealed a statistically significant increase of 0.8 ± 0.5 Tg yr^{-2} (95% confidence interval), of which 0.7 ± 0.7 Tg yr^{-2} is attributed to the anthropogenic sources (Figs. 2e and 2f). The trend changes underscore the dominant role of anthropogenic activity in driving China's CH_4 emissions in recent years, leading to a marked post-2019 increase in total CH_4 fluxes, in contrast to the preceding years. The other independent studies consistently report a similar upward tendency in China's CH_4 emissions after 2019 (Figs. 2e and 2f), although they are typically limited by temporal coverage, often ending before 2022.

It should be noted that our estimated rising trends remain subject to uncertainties, as errors are inevitably introduced by the inversion frameworks, assimilation algorithms, and input datasets. Nevertheless, our findings offer a quantitative assessment of CH_4 emission trends extending through 2024 in China. This result captures a long, continuous, and up-to-date CH_4 emission trajectory, offering updated perspectives on recent emission changes and emphasizing the importance of further investigations into the sectoral and regional drivers responsible for the observed emission growth trend.

https://doi.org/10.5194/egusphere-2025-6284
Preprint. Discussion started: 7 April 2026

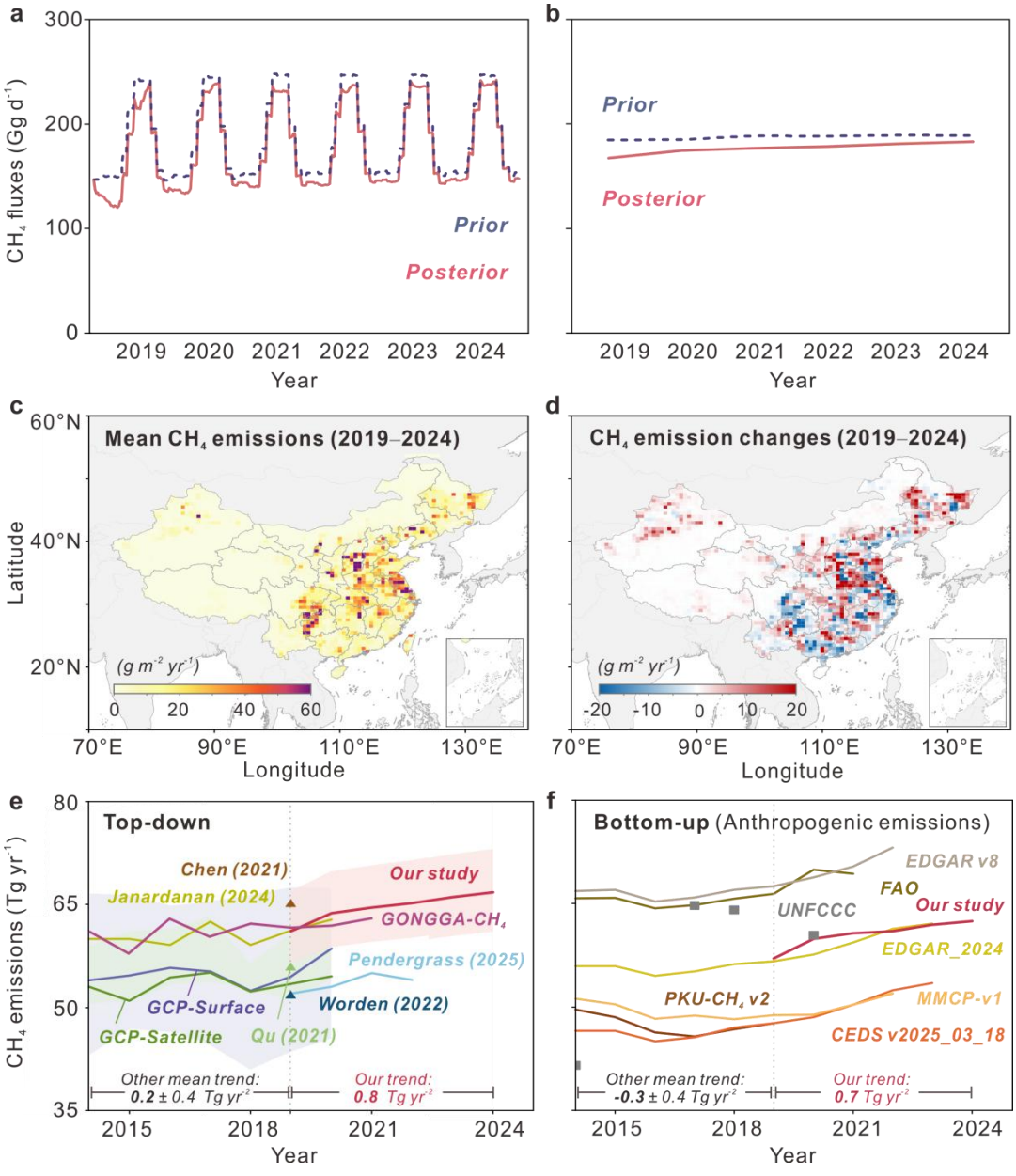

Figure 2: Temporal and spatial distributions of CH_4 fluxes over China and comparisons with other studies. (a and b) Weekly (A) and annual (b) variations of posterior and prior emission fluxes from 2019 to 2024. (c and d) Spatial distribution of mean annual emission fluxes (c) and their changes (d) across China between 2019 and 2024. (e and f) Comparisons of net and anthropogenic CH_4 emissions with top-down (e) and bottom-up studies (f), respectively.

https://doi.org/10.5194/egusphere-2025-6284
Preprint. Discussion started: 7 April 2026

3.3 Drivers of increasing CH_4 emissions in China

To interpret the growth trend of China's CH_4 emissions from 2019 to 2024, we decomposed the posterior total emissions into sectoral contributions based on prior sectoral spatial distribution (Pendergrass et al., 2023). The sectoral categorization, along with the annual average emissions and their annual changes over this period, are summarized in Table 2 and Fig. 3. Coal mining is the dominant emission source, accounting for 27.9% of China's total emissions. This is followed by agricultural activities, with rice cultivation and livestock contributing 19.7% and 13.4%, respectively. Waste treatment also plays an important role, with China's total emissions comprising 13.4% from wastewater and 8.2% from landfills. Natural sources, mainly wetlands and reservoirs, accounted for only 9.0% of China's total emissions.

We attribute the 5.7 Tg increase in CH_4 emissions between 2019 and 2024 primarily to the growth in the livestock sector (+2.7 Tg), with additional contributions from landfills (+0.8 Tg), wastewater (+0.7 Tg), and oil and gas systems (+0.6 Tg). These increases offset the reductions from coal mining (-0.4 Tg), leading to a net growth in China's total CH_4 emissions during the periods. Moving beyond the overall emission structure, identifying sector-specific drivers is key to interpreting recent CH_4 emission changes and guiding targeted mitigation efforts, as discussed below.

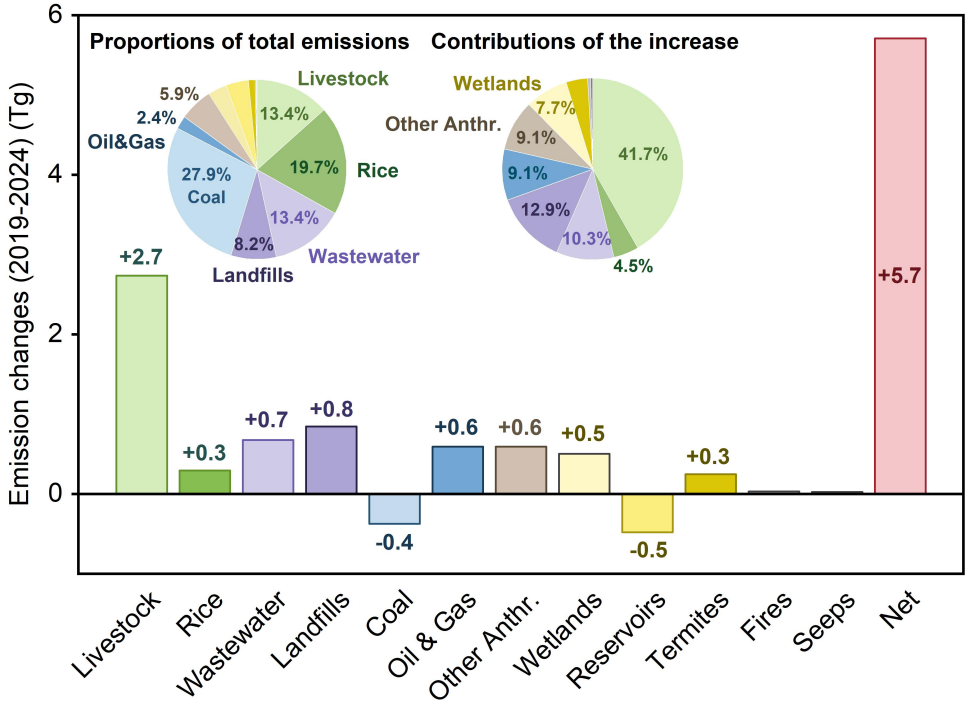

Figure 3: Sectoral CH_4 emissions and their changes in China from 2019 to 2024. Bars show five-year emission changes by sector. Pie charts indicate sectoral shares of total emissions (left) and their relative contributions to the overall emission increase (right), respectively.

https://doi.org/10.5194/egusphere-2025-6284
Preprint. Discussion started: 7 April 2026

3.3.1 Livestock dominates CH_4 emissions growth during 2019–2024

Livestock is the largest contributor to the China's CH_4 emission rise during 2019–2024, despite comprising only 13.4% of the overall emissions (Fig. 3). Over this period, livestock emissions increased at a rate of 0.5 ± 0.1 Tg yr^{-2} (non-parametric Mann-Kendall test, 95% confidence interval), representing a 36.9% increase relative to the 2019 level and accounting for 41.7% of the total emission growth. This contrasts with the declining trends before 2019 from multiple estimates (Crippa, 2024; Du et al., 2024; Peng et al., 2016; Liu et al., 2021; Wang et al., 2024) (Fig. S3), signifying an emerging change in the role of the livestock sector—from a diminishing source to the key driver of recent CH_4 emission growth in China.

Ruminant livestock dominates CH_4 emissions from the livestock sector through enteric fermentation and manure management. Multiple factors, such as fluctuations in the pork market (You et al., 2021), a diversifying trend in national dietary preferences (Gao et al., 2023), and the implementation of livestock industry action plans (China, 2021, 2022), have collectively stimulated the increased consumption of ruminant products. This has accelerated the growth of beef cattle, dairy cattle, and sheep populations, contributing to the recent upward trend in CH_4 emissions (National Bureau of Statistics of China, 2024). The national cattle population increased by approximately 10% from 2019 to 2024, following a relatively stable period from 2013 to 2018 (Fig. S3). Sheep populations, meanwhile, expanded by close to 10% during 2019–2022, which could also stimulate the rise in livestock CH_4 emissions (National Bureau of Statistics of China, 2024).

In addition, pigs, which recently contribute about 20% of the livestock emissions (Du et al., 2024; Wang et al., 2024)—through manure management—also have an important influence on the livestock CH_4 emission changes. Pig population started to decrease around 2015 as the Chinese government introduced non-livestock production regions and pig-reallocation policies to control water pollution (Bai et al., 2019). This decline was further exacerbated by the African Swine Fever outbreak in 2018, which corresponded with a 27.5% reduction in the pig population in 2019 (You et al., 2021). In response, a suite of government interventions that aimed at stabilizing pork supply and prices triggered a rapid recovery in pig numbers. From 2019 to 2020, the pig numbers surged by 31.0%, culminating in a 37.7% increase over 2019–2024 (National Bureau of Statistics of China, 2024). Pig population growth contributed to the livestock emission increase after 2019, partially reversing the emission decline trend observed between 2013 and 2018 (Du et al., 2024; Crippa, 2024). The strengthening of livestock production remains essential for ensuring food security and improving dietary protein supply in China, yet it also needs to be accompanied by comprehensive, targeted strategies to control the consequent rise in CH_4 emissions.

3.3.2 Energy transition curbs fossil fuel emissions growth after 2020

The fossil fuel sector, which emitted over 30% of CH_4 in China during 2019–2024 (Fig. 3), exhibited an increase in 2019 followed by a sustained decline after 2020. Over the study period, the coal mining sector remains the largest emission source in China, averaging 18.6 Tg yr^{-1}, substantially higher than 1.6 Tg yr^{-1} from the oil and gas sector. However, the emission rise

https://doi.org/10.5194/egusphere-2025-6284
Preprint. Discussion started: 7 April 2026

in oil and gas of +0.6 Tg offset the coal emission reduction of -0.4 Tg. Coal emissions increased by 1.0 Tg between 2019 and 2020, and declined steadily by -0.3 ± 0.2 Tg yr^{-2} after 2020, achieving a cumulative reduction of 1.4 Tg over the 2020–2024 period (Fig. S4). Although coal mine CH_4 emission control started in the 2000s (Emission Standard of Coalbed Methane/Coal Mine Gas (on Trial) (Gb 21522—2008), 2008), some key coal CH_4 sources still demand stricter regulatory measures, illustrated by emissions increase in 2019 (Figs. S2 and S4). From 2020 onward, the intensification of emission reduction ultimately outpaced the residual emissions growth, driving a sustained decline in coal CH_4 emissions. Notably, alongside this emission decline, coal production continuously expanded at an average annual rate of 3.8% yr^{-1} (National Bureau of Statistics of China, 2024), indicating a decoupling between coal mining CH_4 emissions and coal production. This decoupling is achieved by multiple synergistic factors, including energy policies on closing down small coal mines and consolidation of large, efficient mines, and the shifts of coal production from high-emitting regions to low-emitting regions, along with the technology advancements in coal mine extraction and CH_4 utilization and recovery (Zhang et al., 2022; Sheng Kai and Hong, 2001; Jiang Lin et al., 2025; China, 2023; Environment; and Regulation, 2024).

Meanwhile, under the ongoing energy structure transition in China, oil and natural gas infrastructures have been expanding to meet the increasing energy demand. The oil and natural gas systems contributed only 2.4% of China's total CH_4 emissions, yet rose by 0.6 Tg between 2019 and 2024—a 47.7% rise relative to the 2019 levels—accounting for 9.1% of the national growth (Fig. 3). These sources mainly include exploration and production, processing, and transmission and storage (Intergovernmental Panel on Climate Change, 2019). From 2019 to 2024, production volumes increased by 40.5% for natural gas and 11.1% for oil (National Bureau of Statistics of China, 2024). The length of oil and gas transmission pipelines increased by nearly 20% (National Bureau of Statistics of China, 2024), indicating that the transmission stage is an important source for the CH_4 emissions rise, particularly for natural gas (Luo et al., 2025). The estimated increasing trend in oil and gas emissions is comparable with the emission inventories, which identify gas exploration, production, and transmission as the major sources of emissions growth in the recent decade (Luo et al., 2025; Crippa, 2024). The ongoing energy transition in China is expected to reduce fossil fuel use and emissions, while the growing demands for oil and gas and the infrastructure pose challenges for China's CH_4 emissions mitigation at present.

3.3.3 Emerging potential for emissions growth from the waste sector

The waste treatment sector (i.e., landfills and wastewater) emitted 14.3 Tg yr^{-1} of CH_4 in China on average over 2019–2024, accounting for around 21.6% of total emissions and contributing 23.2% to the overall increase. Wastewater CH_4 emissions rose from 8.5 Tg yr^{-1} in 2019 to 9.2 Tg yr^{-1} in 2024, primarily from biological treatment processes that remove organics from agricultural, domestic, and industrial wastewater sources (Intergovernmental Panel on Climate Change, 2019; Liu et al., 2024; Jiang Lin et al., 2025; Moore et al., 2025). With the acceleration of social and economic development in China, the total volume of wastewater, along with its corresponding organic content, total chemical oxygen demand (COD), has increased substantially. Particularly in the domestic and agricultural sectors, whose COD generation has risen by 118% and

https://doi.org/10.5194/egusphere-2025-6284
Preprint. Discussion started: 7 April 2026

27%, respectively (National Bureau of Statistics of China, 2024). Consequently, the demand for wastewater treatment has expanded rapidly, which is reflected by the continuous growth of wastewater treatment plants in China from 9,322 in 2019 to 14,620 in 2023 (https://www.mee.gov.cn/hjzl/sthjzk/). Meanwhile, the total urban treatment capacity rose from 19.2 to 23.7 million m^3 per day over the corresponding period, concurrent with the CH_4 emission increase from wastewater treatment. The independent estimates of wastewater emissions align with our trends (Liu et al., 2024; Cui et al., 2025; Chen et al., 2025; Crippa, 2024), highlighting the growing importance of advancing treatment technologies that target wastewater sources to control CH_4 production.

Moreover, China produces a substantial amount of solid waste annually, with landfills long serving as one of the primary disposal methods and a critical CH_4 emission source. Our study observed an increase in landfill CH_4 emissions from 4.9 Tg yr^{-1} in 2019 to 5.8 Tg yr^{-1} in 2024. However, during this period, the volume of solid waste treated by incineration surpassed that disposed of in landfills, with landfill treatment declining due to constraints on landfill expansion and advances in incineration technologies (Fig. S5) (Wang et al., 2023). The inconsistent trends—declining amounts of landfilled waste but rising CH_4 emissions—could be attributed to the cumulative stock of landfills, which continues to generate and release CH_4, as well as the influences from multiple factors such as waste composition, management practices, and gas recovery. The emission growth gradually slowed as revealed by our estimates, indicating a potential stabilization of landfill CH_4 emissions over the recent years (Fig. S2).

However, the waste-related emission trends are possibly subject to high uncertainties, arising from highly uncertain prior emissions in both magnitude and spatial distribution due to complex mechanisms for diverse influencing factors in China's waste sectors. In addition, separating landfill and wastewater emission sources remains highly uncertain due to their close geographic distribution and the coarse spatial resolution of our inversion relative to the source scales. Incorporating fine-resolution and dynamically updated prior inputs, together with optimizing inversion techniques and emission distribution patterns, is necessary to enhance the robustness and reliability of the estimates of waste emissions in future inversions.

3.4 Spatial distribution of China's CH_4 emissions

Given the strong spatial heterogeneity of CH_4 emission magnitudes and changes in China (Figs. 2c, 2d, S6, and S7), quantifying the regional distribution and underlying local drivers is critical for characterizing emission hotspots and for developing, implementing, and evaluating targeted mitigation strategies. We aggregated emissions into six regions (Fig. S1 and Table S1), and found that the highest emission fluxes were observed from East China (15.2 Tg yr^{-1}), followed by South (13.8 Tg yr^{-1}), Southwest (11.7 Tg yr^{-1}), and North China (10.4 Tg yr^{-1}) from 2019 to 2024 (Fig. 4a).

The high emissions from East and South China are primarily due to extensive rice cultivation activity, which contributed roughly one-third of the total emissions in each region. In East China, waste-related emissions are also crucial due to high urbanization, socioeconomic development, and dense population. From 2019 to 2024, the CH_4 emission trend in East China has remained relatively stable, consistent with the steady activity data of major emission sources. In comparison, CH_4

https://doi.org/10.5194/egusphere-2025-6284
Preprint. Discussion started: 7 April 2026

emissions from South China exhibited an increase of 1.3 Tg from 2019 to 2024, driven by intensifying rice cultivation and livestock production, highlighting the urgent need for targeted mitigation measures on agricultural emission sources in South China.

For North and Southwest China, the coal sector is the dominant source of CH_4 emissions, accounting for approximately 60% and 40% of the regional totals, respectively. Shanxi Province is the largest CH_4 emitter in North China, with annual emissions of 16.5 Tg yr^{-1}. Coal mining in Shanxi emitted nearly 89% of its total CH_4 and also contributes nearly 30% of national coal mine CH_4 emissions (Fig. 4b). Shanxi's coal emissions increased between 2019 and 2020, stabilized thereafter, and declined from 2023. This trend governed coal CH_4 emissions across North China, and drove nearly one third of the overall variations in the regional total CH_4 emissions (Figs. 4 and S8). As for Southwest China, Guizhou and Sichuan Provinces are major contributors to coal mining CH_4 emissions. Guizhou exhibited a substantial declining trend in coal emissions before 2022, while Sichuan began a more moderate decline thereafter. These changes collectively drive the regional coal emission decrease and largely influence the overall regional CH_4 emission trends (Figs. 4 and S9).

CH_4 fluxes from Northeast and Northwest China remained relatively low, with mean values of approximately 5.9 Tg yr^{-1} and 7.6 Tg yr^{-1} between 2019 and 2024, respectively, corresponding to 9.1% and 11.8% of the national total. However, both regions exhibited the largest increases from 2019 to 2024 (Fig. 4c). In Northwest China, emissions increased by 2.7 Tg during this period, with approximately 60% of this growth attributed to Xinjiang Province (Figs. 4d and S7). Livestock activity in this region has also expanded, largely driven by government policies aimed at boosting rural incomes. This expansion, particularly in sheep and beef cattle industries, has critically shaped regional livestock emissions and the recent continuous growth (Wang et al., 2024). In addition, Northwest China hosts major oil and natural gas fields, accounting for nearly half of the CH_4 emissions from oil and natural gas systems in China (Crippa, 2021). With the evolving energy structure in China, a surge in oil and gas production in this region makes it the second-largest contributor to CH_4 emission growth in Northwest China. The oil and gas sector in Northwest China should therefore be prioritized for targeted mitigation measures.

In Northeast China, CH_4 emissions climbed by 1.9 Tg during the 6 years, with the most notable rise occurring before 2021 (Fig. 4c). Although extensive rice paddies are distributed in East and South China, there is a potential and ongoing shift in national rice distribution toward the Northeast China, resulting in rice cultivation emerging as the dominant contributor to this regional emissions increase (Shen et al., 2024). This increase is largely concentrated in Heilongjiang Province (Fig. 4d), where CH_4 emissions nearly doubled from 0.4 Tg in 2019 to 0.9 Tg in 2021, in parallel with an upward trend in rice paddy area and production over the same period (National Bureau of Statistics of China, 2024). In addition to rice cultivation, rising emissions from waste treatment and livestock sectors also contributed to the rise in CH_4 emissions over Northeast China.

https://doi.org/10.5194/egusphere-2025-6284
Preprint. Discussion started: 7 April 2026

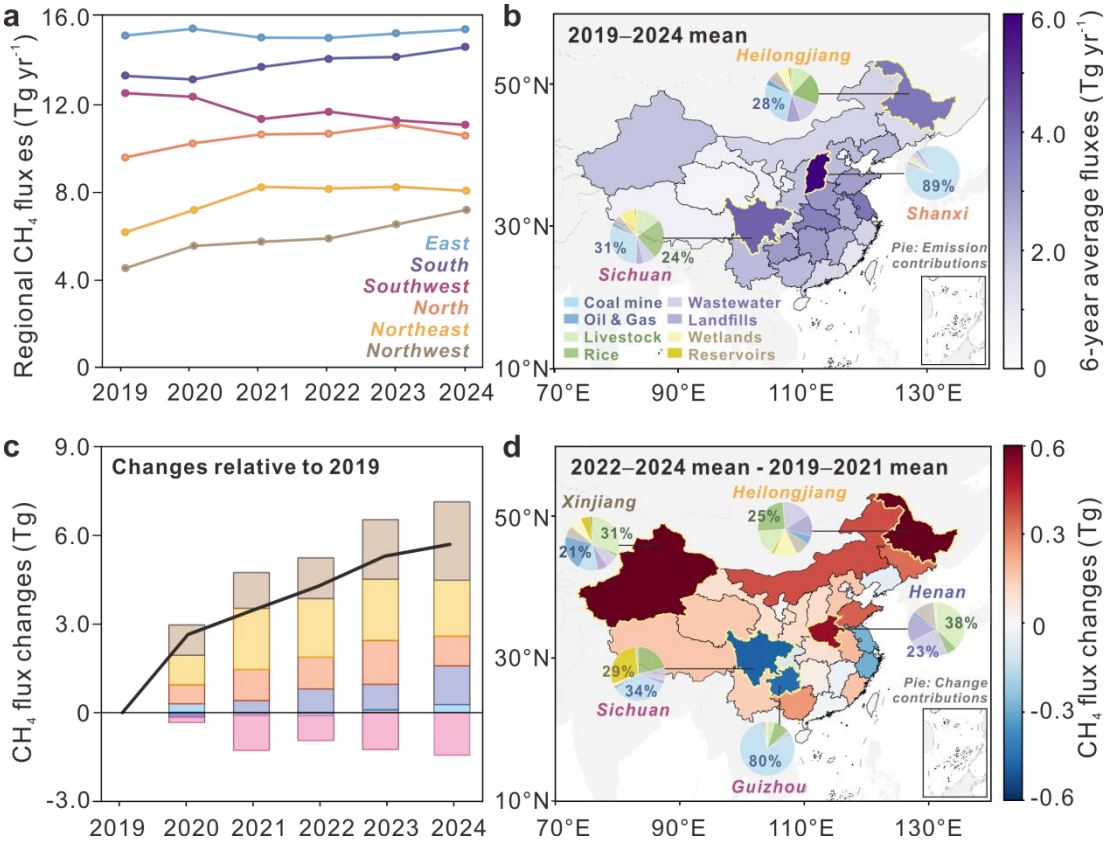

Figure 4: Regional and provincial CH_4 emissions fluxes and their changes over China from 2019 to 2024. (a) Annual CH_4 fluxes by region from 2019 to 2024. (b) Mean provincial CH_4 fluxes distributions during 2019–2024, with pie charts showing sectoral contributions in key provinces. (c) Regional CH_4 flux anomalies relative to 2019 levels. (d) Provincial CH_4 flux changes, calculated as the difference between the 2022–2024 and 2019–2021 means, with pie charts illustrating sectoral contributions to the changes in key provinces. The regional divisions follow Table S1 and Fig. S1, comprising the Northwest, Northeast, Southwest, East, South, and North China.

3.5 Sensitivity analysis of emission inversion

To evaluate the robustness of our inversion results and quantify uncertainty, we performed sensitivity experiments by perturbing key parameters and testing alternative configurations relative to the baseline inversion (Table 3). The estimated average CH_4 fluxes for 2019–2024 across these sensitivity tests varied between -8.0% and +9.3% (Fig. 5) relative to the base case (59.4–70.6 Tg yr^{-1}; mean 64.6 Tg yr^{-1}).

Among the tests, the setting of boundary conditions in the GEOS-Chem simulation and prior errors in the LETKF data assimilation exerted the most pronounced influences on the estimated emissions. We compared results using boundary conditions scaled by a global CH_4 inversion based on the CHEEREIO tool (Scaled_BC) (Pendergrass et al., 2025) against those in our base case, which corrected the bias to align well with the satellite data (Estrada et al., 2025). During the study period, CH_4 concentrations simulated in the Scaled_BC test exhibit a mean discrepancy of 8.6 ± 6.5 ppb compared to satellite

https://doi.org/10.5194/egusphere-2025-6284
Preprint. Discussion started: 7 April 2026

observations, substantially larger than the -0.1 ± 5.5 ppb discrepancy in our base case. Higher biases in the scaled boundary conditions led to notable discrepancies in weekly emission flux estimates relative to the base case (Fig. S10), with a particularly substantial annual mean deviation of -22.6% observed in 2023. These results underscore the importance of accurately representing boundary concentration fields in regional-scale inversions for the long-lived CH_4.

In addition, the specification of prior errors is crucial in the LETKF assimilation process, as it determines the perturbation level and the relative weighting between the prior information and satellite observations. The sensitivity tests are conducted in our study with initial correlated spreads of 0.05 and 0.5 to represent a range from narrow to broad uncertainties for prior inputs (Table 3). Compared to our base setting of 0.15 based on the previous work (Pendergrass et al., 2025), annual estimates of Spread_0.5 and Spread_0.05 tests vary from 11.2% to -6.0% (Fig. S11). Larger prior uncertainties may lead to larger corrections driven by strong satellite signals in localized hotspots. Compared with the negative adjustments in the base and most other tests, the annual relative corrections to the prior input of the Spread_0.5 test turned positive after 2020 and reached up to 7.3% in 2024. Whereas overly small settings on prior errors reduce the inversion's responsiveness to localized satellite observation enhancements. The average relative correction to the prior input during 2019–2024 was -5.6% in the base test, while -8.0% in Spread_0.05. The limited number of sensitivity tests on the prior setting still leaves uncertainty in the estimated results. More careful consideration of prior error specification is required in future inversion studies.

Sensitivity tests consistently confirmed the emission increase trend after 2019 (Fig. 5a), except for the Spread_0.05 and Scaled_BC cases. The emission ratios comparing 2024 to 2019 exhibited a range of 1.06–1.15 across all tests, with livestock emissions remaining the dominant driver of emission increases (Figs. 5b and 5c). These results indicate that reducing livestock CH_4 emissions is a priority initiative for CH_4 mitigation in China at present. Besides, the sensitivity test using different boundary conditions not only produced large differences in annual CH_4 emission magnitudes but also led to notable divergent trends and the associated sectoral drivers. In the Scaled_BC case, a reduction of 4.1 Tg in coal mine emissions primarily drives the overall emission decline. While livestock emissions had previously been increasing, a reversal after 2020 also contributed to the downward trend. These findings further highlight the substantial influence of boundary conditions on the trends, spatiotemporal distributions, and sectoral attribution of regional-scale CH_4 inversions.

https://doi.org/10.5194/egusphere-2025-6284
Preprint. Discussion started: 7 April 2026

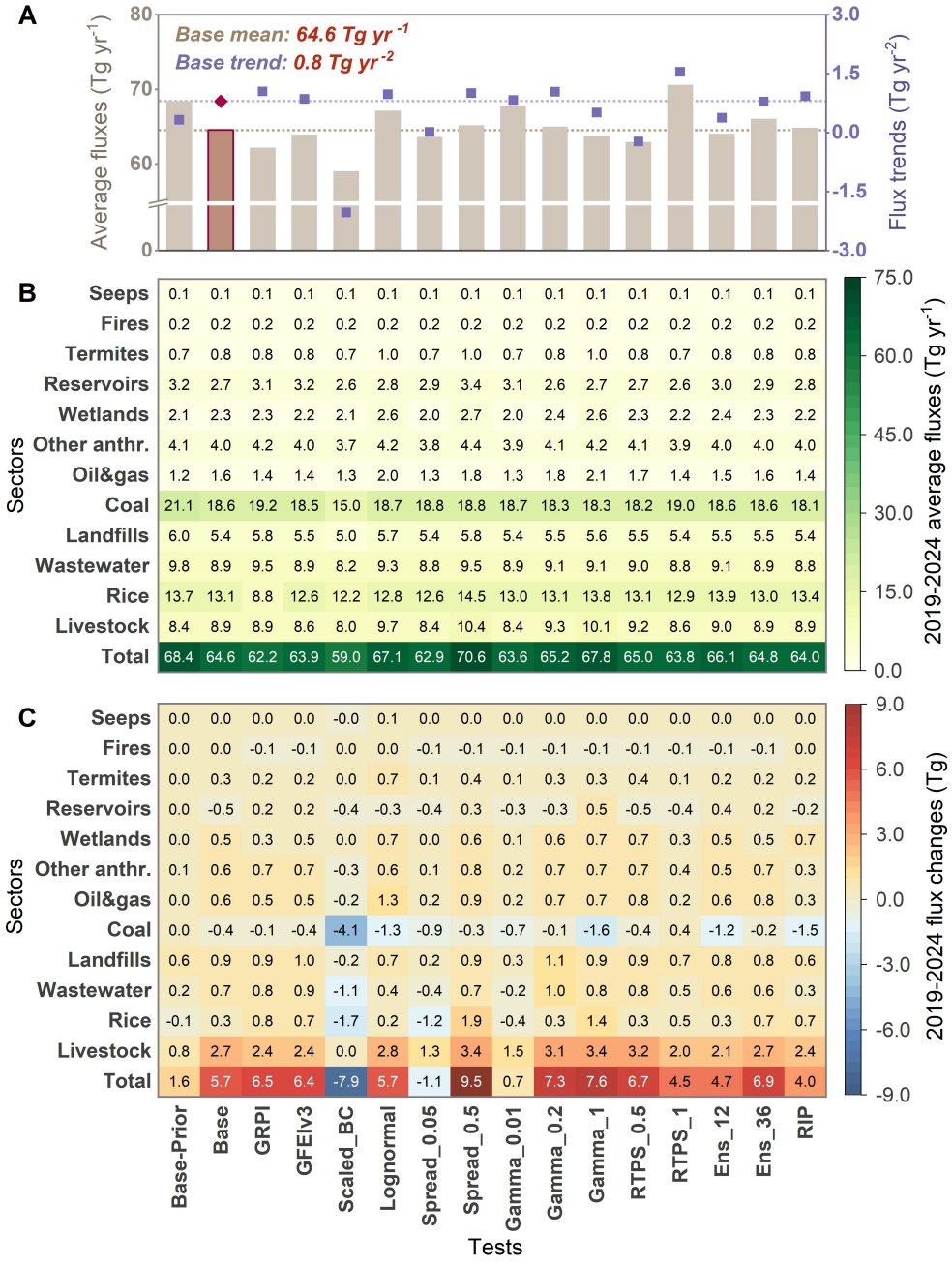

Figure 5: Sensitivity analysis of China's CH_4 inversion results on emission magnitudes and trends. (A) Mean CH_4 emission fluxes and corresponding annual trends were derived for each sensitivity experiment from 2019 to 2024. The trends are calculated by the nonparametric Mann-Kendall test. (B) Mean annual total and sectoral CH_4 fluxes during 2019–2024 for each sensitivity test. (C) Total and sectoral CH_4 emission changes between 2019 and 2024 for each sensitivity test. Details of the test configurations are provided in Table 3. Note that the Scaled_BC test covers the period 2019–2023 only.

https://doi.org/10.5194/egusphere-2025-6284
Preprint. Discussion started: 7 April 2026

4 Conclusions

Our study developed a regional atmospheric inversion framework that is integrated with the LETKF data assimilation algorithm based on the CHEEREIO tool (Pendergrass et al., 2025; Pendergrass et al., 2023) to perform a regional-scale CH_4 flux inversion. We optimized China's CH_4 emissions from 2019 to 2024 at 0.5° × 0.625° spatial resolution and weekly temporal scale by using bias-corrected TROPOMI CH_4 observations. This approach enables tracking of emission changes and drivers with high computational efficiency and supports the construction of national CH_4 MRV systems. We conducted multiple sensitivity tests and confirmed the reliability and robustness of this regional inversion system, and highlighted the importance of selecting appropriate boundary conditions and accurately quantifying prior errors. This regional-scale inversion system development provides valuable and detailed insights for enhancing regional inversion capability and lays a foundation for its future application in real-time monitoring of CH_4 emissions, as well as for extending the inversion to other regions and trace gases.

China's CH_4 emissions rose steadily from 61.1 (56.2–66.7) Tg in 2019 to 66.8 (61.5–73.0) Tg in 2024. Our estimates are broadly consistent with existing studies and strengthen the robustness of the post-2019 emissions growth tendency signal. This growth is largely driven by anthropogenic sources, which contributed 0.6 Tg yr^{-2} of the total 0.7 Tg yr^{-2} emission increase. Livestock emissions, which increased by 36.9% relative to 2019 levels, emerged as the dominant growth driver with a 41.7% contribution. This increase fully offset the emission reduction in the coal mining sector resulting from energy transition and technology improvement, underscoring livestock as a new priority for targeted CH_4 mitigation in China. Additional mitigation opportunities arise from the growing contribution of the waste sectors, which account for 23.2% of the total increase, as well as from oil and natural gas systems contributing 9.1%.

Divergent sectoral emission trajectories drove shifts in the regional emission landscape. From 2019 to 2024, emissions remain highest in the East (23.5% of the total), South (21.4%), Southwest (18.1%), and North China (16.1%). However, Northwest and Northeast China—the lowest-emissions regions accounting for 9.1% and 11.8% of total emissions—are the largest contributors, collectively responsible for 63.8% of the total national CH_4 emissions growth. Therefore, beyond reinforcing emission controls in traditional high-emission regions, targeted mitigation strategies should be developed to focus on livestock and oil-gas emissions in Northwest China, as well as the rice emissions in Northeast China.

Nevertheless, limitations remain in our CH_4 inversion. Several key sectors exhibit large uncertainties in their prior inputs, with substantial discrepancies among different datasets (e.g., rice cultivation; Fig. S12). In addition, prior inventories for some sectors lack sufficient spatial detail, exhibit limited temporal variability, and are updated infrequently. For instance, the GFEI fossil fuel inventory provides only annual mean emissions for a single reference year, without interannual or intra-annual variation. The influence of prior emissions needs to be fully evaluated, particularly regarding how their magnitudes and spatial-temporal patterns affect the posterior results. Furthermore, uncertainties in the magnitude and trends of CH_4 sinks, the choice of CTMs, and the different model settings, such as the spatial resolution and meteorological fields, can also

https://doi.org/10.5194/egusphere-2025-6284
Preprint. Discussion started: 7 April 2026

introduce additional errors. In addition, sensitivity analyses of prior inputs' influence on inversion results remain limited to several key emission sectors and a few databases. Future work should expand these analyses to include all emission sectors and total emissions, incorporating multiple independent datasets to quantify the associated uncertainties more robustly.

Code and data availability

The code of the CHEEREIO tool is available at https://github.com/drewpendergrass/CHEEREIO (last access: 15 December 2025) (Pendergrass et al., 2023). GEOS-Chem version 14.3.1 source code is available at https://zenodo.org/records/10908999 (last access: 15 December 2025) (Yantosca et al., 2024). The blended TROPOMI+GOSAT product is available at https://registry.opendata.aws/blended-tropomi-gosat-methane/ (last access: 15 December 2025) (Balasus et al., 2023). Weekly gridded posterior CH_4 emissions are available at https://figshare.com/s/a47f805000eaf90bc3c7. Additional data used in the inversion and needed to evaluate the conclusions are present in the paper and/or the Supplementary Materials.

Supplement link

The link to the supplement will be included by Copernicus, if applicable.
Figures S1 to S12
Tables S1 to S3

Acknowledgments

The blended TROPOMI+GOSAT data were supported by Nicholas Balasus, and the corresponding corrected boundary conditions by Lucas A. Estrada. We gratefully acknowledge the Atmospheric Chemistry Modeling Group at Harvard University for valuable discussions.

Disclaimer

Publisher's note: Copernicus Publications remains neutral with regard to jurisdictional claims made in the text, published maps, institutional affiliations, or any other geographical representation in this paper. While Copernicus Publications makes every effort to include appropriate place names, the final responsibility lies with the authors.

https://doi.org/10.5194/egusphere-2025-6284
Preprint. Discussion started: 7 April 2026

Financial support

This work was supported by: National Key R&D Program of China (Grant No. 2023YFC3705601), National Natural Science Foundation of China (Grant No. 42375096), and Tsinghua-Toyota Joint Research Institute Cross-Discipline Program.

Author contributions

BZ was responsible for the conceptualization of the study and acquired the funding for this research. The methodology was developed by DP, YL, DJ, YT, and JQ. YL and BZ conducted the investigation and carried out the data collection. YL prepared the visualizations. BZ and DJ supervised the research process. YL wrote the original draft of the manuscript. DP, DJ, BZ, and YL reviewed and edited the manuscript.

Competing interests

The contact author has declared that none of the authors has any competing interests.

Review statement

The review statement will be added by Copernicus Publications, listing the handling editor as well as all contributing referees according to their status, anonymous or identified.

References

Bai, Z., Jin, S., Wu, Y., Ermgassen, E. z., Oenema, O., Chadwick, D., Lassaletta, L., Velthof, G., Zhao, J., and Ma, L.: China's pig relocation in balance, Nature Sustainability, 2, 888-888, 10.1038/s41893-019-0391-2, 2019.

Balasus, N., Jacob, D. J., Lorente, A., Maasakkers, J. D., Parker, R. J., Boesch, H., Chen, Z., Kelp, M. M., Nesser, H., and Varon, D. J.: A blended TROPOMI+GOSAT satellite data product for atmospheric methane using machine learning to correct retrieval biases, Atmos. Meas. Tech., 16, 3787-3807, 10.5194/amt-16-3787-2023, 2023.

Bisht, J. S. H., Patra, P. K., Takigawa, M., Sekiya, T., Kanaya, Y., Saitoh, N., and Miyazaki, K.: Estimation of CH4 emission based on an advanced 4D-LETKF assimilation system, Geosci. Model Dev., 16, 1823-1838, 10.5194/gmd-16-1823-2023, 2023.

Chen, Y., Li, H., and Lu, L.: Methane emissions from industrial wastewater treatment systems decoupling from industrial growth in China over the past two decades, npj Climate and Atmospheric Science, 8, 181, 10.1038/s41612-025-01074-0, 2025.

Chen, Z. and Jacob, D.: Global Rice Paddy Inventory (GRPI): a high-resolution inventory of methane emissions from rice agriculture based on Landsat satellite inundation data (v1.0) [dataset], https://doi.org/10.5281/zenodo.15210212, 2025.

Chen, Z., Jacob, D. J., Nesser, H., Sulprizio, M. P., Lorente, A., Varon, D. J., Lu, X., Shen, L., Qu, Z., Penn, E., and Yu, X.: Methane emissions from China: a high-resolution inversion of TROPOMI satellite observations, Atmos. Chem. Phys., 22, 10809-10826, 10.5194/acp-22-10809-2022, 2022.

Chen, Z., Jacob, D. J., Gautam, R., Omara, M., Stavins, R. N., Stowe, R. C., Nesser, H. O., Sulprizio, M. P., Lorente, A., Varon, D. J., Lu, X., Shen, L., Qu, Z., Pendergrass, D. C., and Hancock, S.: Satellite quantification of methane emissions and

oil/gas methane intensities from individual countries in the Middle East and North Africa: implications for climate action, EGUsphere, 2023, 1-42, 10.5194/egusphere-2022-1504, 2023.
China, M. o. A. a. R. A. o. t. P. s. R. o.: Five-Year Action Plan for Promoting Beef Cattle and Sheep Production (2021–2025), 2021.
China, M. o. A. a. R. A. o. t. P. s. R. o.: Action Plan for Enhancing Dairy Industry Competitiveness during the 14th Five-Year Plan Period, 2022.
China, M. o. E. a. E. o. t. P. s. R. o.: Methane Emission Control Action Plan, 2023.
Crippa, M., Guizzardi, D., Pagani, F., Banja, M., Muntean, M., Schaaf E., Becker, W., Monforti-Ferrario, F., Quadrelli, R., Risquez Martin, A., Taghavi-Moharamli, P., Köykkä, J., Grassi, G., Rossi, S., Brandao De Melo, J., Oom, D., Branco, A., San-Miguel, J., and Vignati, E.: GHG emissions of all world countries, Publications Office of the European Union,, Luxembourg, doi:10.2760/953322, JRC134504., 2023.
Crippa, M., Guizzardi, D., Pagani, F., Banja, M., Muntean, M., Schaaf, E., Monforti-Ferrario, F., Becker, W., Quadrelli, R., Risquez Martin, A., Taghavi-Moharamli, P., Köykkä, J., Grassi, G., Rossi, S., Melo, J., Oom, D., Branco, A., San-Miguel, J., Manca, G., Pisoni, E., Vignati, E. and Pekar, F.: GHG emissions of all world countries, Publications Office of the European Union, Luxembourg, doi:10.2760/4002897, 2024.
Crippa, M., Guizzardi, D., Solazzo, E., Muntean, M., Schaaf, E., Monforti-Ferrario, F., Banja, M., Olivier, J.G.J., Grassi, G., Rossi, S., Vignati, E.: GHG emissions of all world countries - 2021 Report, Publications Office of the European Union, Luxembourg, 10.2760/173513, 2021.
Cui, D., Yang, S., Song, X., Huang, X., Duan, C., Ji, M., Li, Z., Yu, S., Deng, Z., Ke, P., Dou, X., Sun, T., and Liu, Z.: Monthly methane emissions in Chinese mainland provinces from 2013–2022, Scientific Data, 12, 948, 10.1038/s41597-025-05107-4, 2025.
Delwiche, K. B., Harrison, J. A., Maasakkers, J. D., Sulprizio, M. P., Worden, J., Jacob, D. J., and Sunderland, E. M.: Estimating Drivers and Pathways for Hydroelectric Reservoir Methane Emissions Using a New Mechanistic Model, Journal of Geophysical Research: Biogeosciences, 127, e2022JG006908, https://doi.org/10.1029/2022JG006908, 2022.
Du, M., Kang, X., Liu, Q., Du, H., Zhang, J., Yin, Y., and Cui, Z.: City-level livestock methane emissions in China from 2010 to 2020, Scientific Data, 11, 251, 10.1038/s41597-024-03072-y, 2024.
East, J. D., Jacob, D. J., Jervis, D., Balasus, N., Estrada, L. A., Hancock, S. E., Sulprizio, M. P., Thomas, J., Wang, X., Chen, Z., Varon, D. J., and Worden, J. R.: Worldwide inference of national methane emissions by inversion of satellite observations with UNFCCC prior estimates, Nature Communications, 16, 11004, 10.1038/s41467-025-67122-8, 2025.
East, J. D., Jacob, D. J., Balasus, N., Bloom, A. A., Bruhwiler, L., Chen, Z., Kaplan, J. O., Mickley, L. J., Mooring, T. A., Penn, E., Poulter, B., Sulprizio, M. P., Worden, J. R., Yantosca, R. M., and Zhang, Z.: Interpreting the Seasonality of Atmospheric Methane, Geophysical Research Letters, 51, e2024GL108494, https://doi.org/10.1029/2024GL108494, 2024.
Emission Standard of Coalbed Methane/Coal Mine Gas (on Trial) (GB 21522—2008): Emission Standard of Coalbed Methane/Coal Mine Gas（on trial）, 2008.
Environment;, M. o. E. a. and Regulation, S. A. f. M.: Emission standard of coalbed methane （coal mine gas）, 2024.
Eskes, H. J., Velthoven, P. F. J. V., Valks, P. J. M., and Kelder, H. M.: Assimilation of GOME total-ozone satellite observations in a three-dimensional tracer-transport model, Quarterly Journal of the Royal Meteorological Society, 129, 1663-1681, https://doi.org/10.1256/qj.02.14, 2003.
Estrada, L. A., Varon, D. J., Sulprizio, M., Nesser, H., Chen, Z., Balasus, N., Hancock, S. E., He, M., East, J. D., Mooring, T. A., Oort Alonso, A., Maasakkers, J. D., Aben, I., Baray, S., Bowman, K. W., Worden, J. R., Cardoso-Saldaña, F. J., Reidy, E., and Jacob, D. J.: Integrated Methane Inversion (IMI) 2.0: an improved research and stakeholder tool for monitoring total methane emissions with high resolution worldwide using TROPOMI satellite observations, Geosci. Model Dev., 18, 3311-3330, 10.5194/gmd-18-3311-2025, 2025.
Etiope, G., Ciotoli, G., Schwietzke, S., and Schoell, M.: Gridded maps of geological methane emissions and their isotopic signature, Earth Syst. Sci. Data, 11, 1-22, 10.5194/essd-11-1-2019, 2019.
FAOSTAT Climate Change: Agrifood systems emissions; Emissions from
Energy use in agriculture: http://www.fao.org/faostat/en/#data/GN, last
Food and Agriculture Organization of the United Nations: FAOSTAT [dataset], 2025.

https://doi.org/10.5194/egusphere-2025-6284
Preprint. Discussion started: 7 April 2026

Fung, I., John, J., Lerner, J., Matthews, E., Prather, M., Steele, L. P., and Fraser, P. J.: Three-dimensional model synthesis of the global methane cycle, Journal of Geophysical Research: Atmospheres, 96, 13033-13065, https://doi.org/10.1029/91JD01247, 1991.
Gao, Q., Liu, H., Wang, Z., Lan, X., An, J., Shen, W., and Wan, F.: Recent advances in feed and nutrition of beef cattle in China - A review, Anim Biosci, 36, 529-539, 10.5713/ab.22.0192, 2023.
Gaspari, G. and Cohn, S. E.: Construction of correlation functions in two and three dimensions, Quarterly Journal of the Royal Meteorological Society, 125, 723-757, https://doi.org/10.1002/qj.49712555417, 1999.
Global Methane Pledge: Global Methane Pledge, 2023.
Guo, F., Dai, F., Gong, P., and Zhou, Y.: CHN-CH4: A Gridded (0.1°×0.1°) Anthropogenic Methane Emission Inventory of China from 1990 to 2020, Earth Syst. Sci. Data Discuss., 2025, 1-25, 10.5194/essd-2025-178, 2025.
Hmiel, B., Petrenko, V. V., Dyonisius, M. N., Buizert, C., Smith, A. M., Place, P. F., Harth, C., Beaudette, R., Hua, Q., Yang, B., Vimont, I., Michel, S. E., Severinghaus, J. P., Etheridge, D., Bromley, T., Schmitt, J., Faïn, X., Weiss, R. F., and Dlugokencky, E.: Preindustrial (14)CH(4) indicates greater anthropogenic fossil CH(4) emissions, Nature, 578, 409-412, 10.1038/s41586-020-1991-8, 2020.
Hoesly, R., Smith, S. J., Ahsan, H., Prime, N., O'Rourke, P., Crippa, M., Klimont, Z., Guizzardi, D., Feng, L., Harkins, C., MCDONALD, B., & Wang, S. : CEDS v_2025_03_18 Aggregate Data (v_2025_03_18) [dataset], https://doi.org/10.5281/zenodo.15059443, 2025.
Hunt, B. R., Kostelich, E. J., and Szunyogh, I.: Efficient data assimilation for spatiotemporal chaos: A local ensemble transform Kalman filter, Physica D: Nonlinear Phenomena, 230, 112-126, https://doi.org/10.1016/j.physd.2006.11.008, 2007.
Intergovernmental Panel on Climate Change: 2019 Refinement to the 2006 IPCC Guidelines for National Greenhouse Gas Inventories, Kyoto, Japan, 2019.
Intergovernmental Panel on Climate Change: Climate Change 2021 – The Physical Science Basis: Working Group I Contribution to the Sixth Assessment Report of the Intergovernmental Panel on Climate Change, Cambridge University Press, Cambridge, DOI: 10.1017/9781009157896, 2023.
Janardanan, R., Maksyutov, S., Wang, F., Nayagam, L., Sahu, S. K., Mangaraj, P., Saunois, M., Lan, X., and Matsunaga, T.: Country-level methane emissions and their sectoral trends during 2009–2020 estimated by high-resolution inversion of GOSAT and surface observations, Environmental Research Letters, 19, 034007, 10.1088/1748-9326/ad2436, 2024.
Janardanan, R., Maksyutov, S., Tsuruta, A., Wang, F., Tiwari, Y. K., Valsala, V., Ito, A., Yoshida, Y., Kaiser, J. W., Janssens-Maenhout, G., Arshinov, M., Sasakawa, M., Tohjima, Y., Worthy, D. E. J., Dlugokencky, E. J., Ramonet, M., Arduini, J., Lavric, J. V., Piacentino, S., Krummel, P. B., Langenfelds, R. L., Mammarella, I., and Matsunaga, T.: Country-Scale Analysis of Methane Emissions with a High-Resolution Inverse Model Using GOSAT and Surface Observations, Remote Sensing, 12, 375, 2020.
Jiang Lin, Jie Zhang, Bobing Qiu, and Khanna, N.: Regional Production Shift and Increased Utilization Dampen Coal Mine Methane Emissions in China (preprint), https://doi.org/10.21203/rs.3.rs-6550772/v1,
Kalnay, E. and Yang, S.-C.: Accelerating the spin-up of Ensemble Kalman Filtering, Quarterly Journal of the Royal Meteorological Society, 136, 1644-1651, https://doi.org/10.1002/qj.652, 2010.
Kou, X., Peng, Z., Han, X., Li, J., Qin, L., Zhang, M., Parker, R. J., and Boesch, H.: China's methane emissions derived from the inversion of GOSAT observations with a CMAQ and EnKS-based regional data assimilation system, Atmospheric Pollution Research, 16, 102333, https://doi.org/10.1016/j.apr.2024.102333, 2025.
Lan, X., K.W. Thoning, and Dlugokencky, E. J.: Trends in globally-averaged CH4, N2O, and SF6 determined from NOAA Global Monitoring Laboratory measurements (Version 2025-08) [dataset], https://doi.org/10.15138/P8XG-AA10, 2025.
Li, Y. and Zheng, B.: Tracking regional CH4 emissions through collocated air pollution measurement: a pilot application and robustness analysis in China, npj Climate and Atmospheric Science, 8, 127, 10.1038/s41612-025-01011-1, 2025.
Liu, G., Peng, S., Lin, X., Ciais, P., Li, X., Xi, Y., Lu, Z., Chang, J., Saunois, M., Wu, Y., Patra, P., Chandra, N., Zeng, H., and Piao, S.: Recent Slowdown of Anthropogenic Methane Emissions in China Driven by Stabilized Coal Production, Environmental Science & Technology Letters, 8, 739-746, 10.1021/acs.estlett.1c00463, 2021.
Liu, W., Li, N., Gao, P., Di, X., Liu, L., and Li, G. K.: Tracking China's methane emissions from wastewater: Inventories, driving forces, and mitigation potential, Resources, Conservation and Recycling, 210, 107831, https://doi.org/10.1016/j.resconrec.2024.107831, 2024.

https://doi.org/10.5194/egusphere-2025-6284
Preprint. Discussion started: 7 April 2026

Liu, Y., Kalnay, E., Zeng, N., Asrar, G., Chen, Z., and Jia, B.: Estimating surface carbon fluxes based on a local ensemble transform Kalman filter with a short assimilation window and a long observation window: an observing system simulation experiment test in GEOS-Chem 10.1, Geosci. Model Dev., 12, 2899-2914, 10.5194/gmd-12-2899-2019, 2019.

Lorente, A., Borsdorff, T., Butz, A., Hasekamp, O., aan de Brugh, J., Schneider, A., Wu, L., Hase, F., Kivi, R., Wunch, D., Pollard, D. F., Shiomi, K., Deutscher, N. M., Velazco, V. A., Roehl, C. M., Wennberg, P. O., Warneke, T., and Landgraf, J.: Methane retrieved from TROPOMI: improvement of the data product and validation of the first 2 years of measurements, Atmos. Meas. Tech., 14, 665-684, 10.5194/amt-14-665-2021, 2021.

Lu, X., Jacob, D. J., Zhang, Y., Maasakkers, J. D., Sulprizio, M. P., Shen, L., Qu, Z., Scarpelli, T. R., Nesser, H., Yantosca, R. M., Sheng, J., Andrews, A., Parker, R. J., Boesch, H., Bloom, A. A., and Ma, S.: Global methane budget and trend, 2010–2017: complementarity of inverse analyses using in situ (GLOBALVIEWplus CH4 ObsPack) and satellite (GOSAT) observations, Atmos. Chem. Phys., 21, 4637-4657, 10.5194/acp-21-4637-2021, 2021.

Luo, J., Wang, H., Li, H., and Zheng, B.: Structural shifts in China's oil and gas CH4 emissions with implications for mitigation efforts, Nature Communications, 16, 2926, 10.1038/s41467-025-58237-z, 2025.

Ministry of Ecology and Environment of China: Methane Emission Control Action Plan, 2023.

Ministry of Ecology and Environment of China: The People's Republicof China Fourth Biennial Update Report on Climate Change, 2024.

Miyazaki, K., Eskes, H. J., and Sudo, K.: Global NOx emission estimates derived from an assimilation of OMI tropospheric NO2 columns, Atmos. Chem. Phys., 12, 2263-2288, 10.5194/acp-12-2263-2012, 2012.

Moore, D. P., Li, N. P., Song, C., Zhu, J.-J., Yi, H., Tao, L., McSpiritt, J., Sevostianov, V. I., Wendt, L. P., Rojas-Robles, N. E., Hopkins, F. M., Ren, Z. J., and Zondlo, M. A.: Comprehensive assessment of the contribution of wastewater treatment to urban greenhouse gas and ammonia emissions, Nature Water, 3, 1114-1124, 10.1038/s44221-025-00490-z, 2025.

Mooring, T. A., Jacob, D. J., Sulprizio, M. P., Balasus, N., Baier, B. C., Kiefer, M., et al.: Evaluating Stratospheric Methane in GEOS-Chem with Satellite and Balloon Observations, American Meteorological Society 104th Annual Meeting, Baltimore, MD, USA,

Murguia-Flores, F., Arndt, S., Ganesan, A. L., Murray-Tortarolo, G., and Hornibrook, E. R. C.: Soil Methanotrophy Model (MeMo v1.0): a process-based model to quantify global uptake of atmospheric methane by soil, Geosci. Model Dev., 11, 2009-2032, 10.5194/gmd-11-2009-2018, 2018.

National Bureau of Statistics of China: China Statistics Yearbook 2024.

Pendergrass, D. C., Jacob, D. J., Nesser, H., Varon, D. J., Sulprizio, M., Miyazaki, K., and Bowman, K. W.: CHEEREIO 1.0: a versatile and user-friendly ensemble-based chemical data assimilation and emissions inversion platform for the GEOS-Chem chemical transport model, Geosci. Model Dev., 16, 4793-4810, 10.5194/gmd-16-4793-2023, 2023.

Pendergrass, D. C., Jacob, D. J., Balasus, N., Estrada, L., Varon, D. J., East, J. D., He, M., Mooring, T. A., Penn, E., Nesser, H., and Worden, J. R.: Trends and seasonality of 2019–2023 global methane emissions inferred from a localized ensemble transform Kalman filter (CHEEREIO v1.3.1) applied to TROPOMI satellite observations, EGUsphere, 2025, 1-26, 10.5194/egusphere-2025-1554, 2025.

Peng, S., Piao, S., Bousquet, P., Ciais, P., Li, B., Lin, X., Tao, S., Wang, Z., Zhang, Y., and Zhou, F.: Inventory of anthropogenic methane emissions in mainland China from 1980 to 2010, Atmospheric Chemistry and Physics, 16, 14545-14562, 10.5194/acp-16-14545-2016, 2016.

Qu, Z., Jacob, D. J., Shen, L., Lu, X., Zhang, Y., Scarpelli, T. R., Nesser, H., Sulprizio, M. P., Maasakkers, J. D., Bloom, A. A., Worden, J. R., Parker, R. J., and Delgado, A. L.: Global distribution of methane emissions: a comparative inverse analysis of observations from the TROPOMI and GOSAT satellite instruments, Atmospheric Chemistry and Physics, 21, 14159-14175, 10.5194/acp-21-14159-2021, 2021.

Randerson, J. T., Van Der Werf, G. R., Giglio, L., Collatz, G. J., and Kasibhatla, P. S.: Global Fire Emissions Database, Version 4.1 (GFEDv4), 10.3334/ORNLDAAC/1293, 2017.

Saunois, M., Martinez, A., Poulter, B., Zhang, Z., Raymond, P. A., Regnier, P., Canadell, J. G., Jackson, R. B., Patra, P. K., Bousquet, P., Ciais, P., Dlugokencky, E. J., Lan, X., Allen, G. H., Bastviken, D., Beerling, D. J., Belikov, D. A., Blake, D. R., Castaldi, S., Crippa, M., Deemer, B. R., Dennison, F., Etiope, G., Gedney, N., Höglund-Isaksson, L., Holgerson, M. A., Hopcroft, P. O., Hugelius, G., Ito, A., Jain, A. K., Janardanan, R., Johnson, M. S., Kleinen, T., Krummel, P. B., Lauerwald, R., Li, T., Liu, X., McDonald, K. C., Melton, J. R., Mühle, J., Müller, J., Murguia-Flores, F., Niwa, Y., Noce, S., Pan, S., Parker, R. J., Peng, C., Ramonet, M., Riley, W. J., Rocher-Ros, G., Rosentreter, J. A., Sasakawa, M., Segers, A., Smith, S. J.,

https://doi.org/10.5194/egusphere-2025-6284
Preprint. Discussion started: 7 April 2026

Stanley, E. H., Thanwerdas, J., Tian, H., Tsuruta, A., Tubiello, F. N., Weber, T. S., van der Werf, G. R., Worthy, D. E. J., Xi, Y., Yoshida, Y., Zhang, W., Zheng, B., Zhu, Q., Zhu, Q., and Zhuang, Q.: Global Methane Budget 2000–2020, Earth Syst. Sci. Data, 17, 1873-1958, 10.5194/essd-17-1873-2025, 2025.

Saunois, M., Stavert, A. R., Poulter, B., Bousquet, P., Canadell, J. G., Jackson, R. B., Raymond, P. A., Dlugokencky, E. J., Houweling, S., Patra, P. K., Ciais, P., Arora, V. K., Bastviken, D., Bergamaschi, P., Blake, D. R., Brailsford, G., Bruhwiler, L., Carlson, K. M., Carrol, M., Castaldi, S., Chandra, N., Crevoisier, C., Crill, P. M., Covey, K., Curry, C. L., Etiope, G., Frankenberg, C., Gedney, N., Hegglin, M. I., Höglund-Isaksson, L., Hugelius, G., Ishizawa, M., Ito, A., Janssens-Maenhout, G., Jensen, K. M., Joos, F., Kleinen, T., Krummel, P. B., Langenfelds, R. L., Laruelle, G. G., Liu, L., Machida, T., Maksyutov, S., McDonald, K. C., McNorton, J., Miller, P. A., Melton, J. R., Morino, I., Müller, J., Murguia-Flores, F., Naik, V., Niwa, Y., Noce, S., O'Doherty, S., Parker, R. J., Peng, C., Peng, S., Peters, G. P., Prigent, C., Prinn, R., Ramonet, M., Regnier, P., Riley, W. J., Rosentreter, J. A., Segers, A., Simpson, I. J., Shi, H., Smith, S. J., Steele, L. P., Thornton, B. F., Tian, H., Tohjima, Y., Tubiello, F. N., Tsuruta, A., Viovy, N., Voulgarakis, A., Weber, T. S., van Weele, M., van der Werf, G. R., Weiss, R. F., Worthy, D., Wunch, D., Yin, Y., Yoshida, Y., Zhang, W., Zhang, Z., Zhao, Y., Zheng, B., Zhu, Q., Zhu, Q., and Zhuang, Q.: The Global Methane Budget 2000–2017, Earth Syst. Sci. Data, 12, 1561-1623, 10.5194/essd-12-1561-2020, 2020.

Scarpelli, T. R., Roy, E., Jacob, D. J., Sulprizio, M. P., Tate, R. D., and Cusworth, D. H.: Using new geospatial data and 2020 fossil fuel methane emissions for the Global Fuel Exploitation Inventory (GFEI) v3, Earth System Science Data, 2025, 1-23, 10.5194/essd-2024-552, 2025.

Scarpelli, T. R., Jacob, D. J., Grossman, S., Lu, X., Qu, Z., Sulprizio, M. P., Zhang, Y., Reuland, F., Gordon, D., and Worden, J. R.: Updated Global Fuel Exploitation Inventory (GFEI) for methane emissions from the oil, gas, and coal sectors: evaluation with inversions of atmospheric methane observations, Atmospheric Chemistry and Physics, 22, 3235-3249, 10.5194/acp-22-3235-2022, 2022.

Schuldt, K. N., Aalto, T., Andrade, M., Arlyn, A., Apadula, F., Jgor, A., Arnold, S., Baier, B., Bäni, L., Bartyzel, J., Bergamaschi, P., Biermann, T., Biraud, S. C., Pierre-Eric, B., Boenisch, H., Brailsford, G., Brand, W. A., Brunner, D., Bui, T. P. V., Van Den Bulk, P., Benoit, B., Francescopiero, C., Chang, C. S., Huilin, C., Lukasz, C., St. Clair, J. M., Sites, C., Coletta, J. D., Colomb, A., Condori, L., Conen, F., Conil, S., Couret, C., Cristofanelli, P., Cuevas, E., Curcoll, R., Daube, B., Davis, K. J., Dean-Day, J. M., Delmotte, M., Ankur, D., DiGangi, E., DiGangi, J. P., Elsasser, M., Emmenegger, L., Forster, G., Frumau, A., Fuente-Lastra, M., Galkowski, M., Gatti, L. V., Gehrlein, T., Gerbig, C., Francois, G., Gloor, E., Goto, D., Hammer, S., Hanisco, T. F., Haszpra, L., Hatakka, J., Heimann, M., Heliasz, M., Heltai, D., Henne, S., Hensen, A., Hermans, C., Hermansen, O., Hoheisel, A., Holst, J., Di Iorio, T., Iraci, L. T., Ivakhov, V., Jaffe, D. A., Jordan, A., Joubert, W., Kang, H.-Y., Karion, A., Kazan, V., Keeling, R. F., Keronen, P., Kers, B., Jooil, K., Klausen, J., Kneuer, T., Ko, M.-Y., Kolari, P., Kominkova, K., Kort, E., Kozlova, E., Krummel, P. B., Kubistin, D., Kulawik, S. S., Kumps, N., Labuschagne, C., Lan, X., Langenfelds, R. L., Lanza, A., Laurent, O., Laurila, T., Lauvaux, T., Lavric, J., Choong-Hoon, L., Lee, J., Lehner, I., Lehtinen, K., Leppert, R., Leskinen, A., Leuenberger, M., Levin, I., Levula, J., Lindauer, M., Lindroth, A., Mikaell Ottosson, L., Loh, Z. M., Lopez, M., Lowry, D., Lunder, C. R., Machida, T., Mammarella, I., Manca, G., Manning, A., Marek, M. V., Marklund, P., Marrero, J. E., Martin, D., Martin, M. Y., Giordane, A. M., Matsueda, H., De Mazière, M., McKain, K., Meinhardt, F., Menoud, M., Jean-Marc, M., Miles, N. L., Miller, C. E., Miller, J. B., Mölder, M., Monteiro, V., Montzka, S., Moore, F., Moossen, H., Moreno, C., Morgan, E., Josep-Anton, M., Morimoto, S., Müller-Williams, J., Munro, D., Mutuku, M., Myhre, C. L., Jaroslaw, N., Nichol, S., Nisbet, E., Niwa, Y., Njiru, D. M., Noe, S. M., O'Doherty, S., Obersteiner, F., Parworth, C. L., Peltola, O., Peters, W., Philippon, C., Piacentino, S., Pichon, J. M., Pickers, P., Pitt, J., Pittman, J., Plass-Dülmer, C., Platt, S. M., Popa, M. E., Prinzivalli, S., Ramonet, M., Richardson, S. J., Louis-Jeremy, R., Rivas, P. P., Röckmann, T., Rothe, M., Yves-Alain, R., Ju-Mee, R., Santoni, G., Di Sarra, A. G., Sasakawa, M., Schaefer, H., Scheeren, B., Schmidt, M., Schuck, T., Schumacher, M., Seifert, T., Sha, M. K., Shepson, P., Daegeun, S., Sloop, C. D., Smale, D., Smith, P. D., Sørensen, L. L., De Souza, R. A. F., Spain, G., Steger, D., Steinbacher, M., Stephens, B., Sweeney, C., Taipale, R., Takatsuji, S., Thoning, K., Timas, H., Torn, M., Trisolino, P., Turnbull, J., Van Der Veen, C., Vermeulen, A., Viner, B., Vitkova, G., Vitkova, G., De Vries, M., Watson, A., Weiss, R., Weyrauch, D., Wofsy, S. C., Worsey, J., Worthy, D., Xueref-Remy, I., Yates, E. L., Dickon, Y., Yver-Kwok, C., Zaehle, S., Zahn, A., Zazzeri, G., Zellweger, C., and Miroslaw, Z.: Multi-laboratory compilation of atmospheric carbon dioxide data for the period 1983-2023; obspack_ch4_1_GLOBALVIEWplus_v7.0_2024-10-29, NOAA Global Monitoring Laboratory [dataset], 10.25925/20241001, 2024.

https://doi.org/10.5194/egusphere-2025-6284
Preprint. Discussion started: 7 April 2026

Shen, N., Tan, J., Wang, W., Xue, W., Wang, Y., Huang, L., Yan, G., Song, Y., and Li, L.: Long-term changes of methane emissions from rice cultivation during 2000 – 2060 in China: Trends, driving factors, predictions and policy implications, Environment International, 191, 108958, https://doi.org/10.1016/j.envint.2024.108958, 2024.

Sheng Kai, H. and Hong, L.: Notice on Effectively Closing and Rectifying Small Coal Mines and Ensuring Coal Mine Safety Production (in Chinese), 2001.

Staniaszek, Z., Griffiths, P. T., Folberth, G. A., O'Connor, F. M., Abraham, N. L., and Archibald, A. T.: The role of future anthropogenic methane emissions in air quality and climate, npj Climate and Atmospheric Science, 5, 21, 10.1038/s41612-022-00247-5, 2022.

van der Werf, G. R., Randerson, J. T., Giglio, L., van Leeuwen, T. T., Chen, Y., Rogers, B. M., Mu, M., van Marle, M. J. E., Morton, D. C., Collatz, G. J., Yokelson, R. J., and Kasibhatla, P. S.: Global fire emissions estimates during 1997–2016, Earth Syst. Sci. Data, 9, 697-720, 10.5194/essd-9-697-2017, 2017.

Voshtani, S., Jones, D. B. A., Wunch, D., Pendergrass, D. C., Wennberg, P. O., Pollard, D. F., Morino, I., Ohyama, H., Deutscher, N. M., Hase, F., Sussmann, R., Weidmann, D., Kivi, R., García, O., Té, Y., Chen, J., Anderson, K., Stevens, R., Kondragunta, S., Zhu, A., Worthy, D., Racki, S., McKain, K., Makarova, M. V., Jones, N., Mahieu, E., Cadena-Caicedo, A., Cristofanelli, P., Labuschagne, C., Kozlova, E., Seitz, T., Steinbacher, M., Mahdi, R., and Murata, I.: Quantifying CO emissions from boreal wildfires by assimilating TROPOMI and TCCON observations, EGUsphere, 2025, 1-60, 10.5194/egusphere-2025-858, 2025.

Wang, D., Yuan, W., Xie, Y., Fei, X., Ren, F., Wei, Y., Jiao, G., and Li, M.: Simulating CH4 emissions from MSW landfills in China from 2003 to 2042 using IPCC and LandGEM models, Heliyon, 9, e22943, https://doi.org/10.1016/j.heliyon.2023.e22943, 2023.

Wang, X., Jacob, D. J., Eastham, S. D., Sulprizio, M. P., Zhu, L., Chen, Q., Alexander, B., Sherwen, T., Evans, M. J., Lee, B. H., Haskins, J. D., Lopez-Hilfiker, F. D., Thornton, J. A., Huey, G. L., and Liao, H.: The role of chlorine in global tropospheric chemistry, Atmos. Chem. Phys., 19, 3981-4003, 10.5194/acp-19-3981-2019, 2019.

Wang, Y., Zhu, Z., Dong, H., Zhang, X., Wang, S., and Gu, B.: Mitigation potential of methane emissions in China's livestock sector can reach one-third by 2030 at low cost, Nature Food, 5, 603-614, 10.1038/s43016-024-01010-0, 2024.

Wecht, K. J., Jacob, D. J., Frankenberg, C., Jiang, Z., and Blake, D. R.: Mapping of North American methane emissions with high spatial resolution by inversion of SCIAMACHY satellite data, Journal of Geophysical Research: Atmospheres, 119, 7741-7756, https://doi.org/10.1002/2014JD021551, 2014.

Whitaker, J. S. and Hamill, T. M.: Evaluating Methods to Account for System Errors in Ensemble Data Assimilation, Monthly Weather Review, 140, 3078-3089, https://doi.org/10.1175/MWR-D-11-00276.1, 2012.

Worden, J. R., Cusworth, D. H., Qu, Z., Yin, Y., Zhang, Y., Bloom, A. A., Ma, S., Byrne, B. K., Scarpelli, T., Maasakkers, J. D., Crisp, D., Duren, R., and Jacob, D. J.: The 2019 methane budget and uncertainties at 1° resolution and each country through Bayesian integration Of GOSAT total column methane data and a priori inventory estimates, Atmospheric Chemistry and Physics, 22, 6811-6841, 10.5194/acp-22-6811-2022, 2022.

Yantosca, B., Sulprizio, M., Lundgren, L., Keller, C., kelvinhb, Eastham, S. D., Fritz, T., Lin, H., degrees, Ridley, D., Bindle, L., michael s, l., tsherwen, Downs, W., Fisher, J., Thackray, C., Holmes, C., GanLuo, BettyCroft, Zhuang, J., Murray, L., SpaceMouse, Estrada, L. A., Shutter, J., noelleselin, nicholasbalasus, Long, M., xin chen, g., emily, r., and Jourdan, H.: geoschem/geos-chem: GEOS-Chem 14.3.1, Zenodo [code], 2024.

You, S., Liu, T., Zhang, M., Zhao, X., Dong, Y., Wu, B., Wang, Y., Li, J., Wei, X., and Shi, B.: African swine fever outbreaks in China led to gross domestic product and economic losses, Nature Food, 2, 802-808, 10.1038/s43016-021-00362-1, 2021.

Zhang, Y., Fang, S., Chen, J., Lin, Y., Chen, Y., Liang, R., Jiang, K., Parker, R. J., Boesch, H., Steinbacher, M., Sheng, J.-X., Lu, X., Song, S., and Peng, S.: Observed changes in China's methane emissions linked to policy drivers, Proceedings of the National Academy of Sciences, 119, e2202742119, doi:10.1073/pnas.2202742119, 2022.

Zhang, Z., Zimmermann, N. E., Kaplan, J. O., and Poulter, B.: Modeling spatiotemporal dynamics of global wetlands: comprehensive evaluation of a new sub-grid TOPMODEL parameterization and uncertainties, Biogeosciences, 13, 1387-1408, 10.5194/bg-13-1387-2016, 2016.

Zhao, M., Tian, X., Wang, Y., Wang, X., Ciais, P., Jin, Z., Zhang, H., Wang, T., Ding, J., and Piao, S.: Slowdown in China's methane emission growth, National Science Review, 11, 10.1093/nsr/nwae223, 2024.